Highly multiplexed single-cell analysis of formalin-fixed, paraffin-embedded cancer tissue

Michael J. Gerdes[a,1], Christopher J. Sevinsky[b,1], Anup Sood[c,1], Sudeshna Adak[d], Musodiq O. Bello[e,2], Alexander Bordwell[c,3], Ali Can[e], Alex Corwin[f], Sean Dinn[c], Robert J. Filkins[g], Denise Hollman[b,3], Vidya Kamath[h], Sireesha Kaanumalle[c], Kevin Kenny[i], Melinda Larsen[a,4], Michael Lazare[j,3], Qing Li[j], Christina Lowes[j], Colin C. McCulloch[k], Elizabeth McDonough[j], Michael C. Montalto[l,5], Zhengyu Pang[b], Jens Rittscher[m], Alberto Santamaria-Pang[e], Brion D. Sarachan[n], Maximilian L. Seel[b], Antti Seppo[a], Kashan Shaikh[f], Yunxia Sui[k], Jingyu Zhang[b], and Fiona Ginty[o,6]

[a]Cell Biology Laboratory, [b]Biochemistry and Bioanalytics Laboratory, [c]Biological and Organic Chemistry Laboratory, [e]Biomedical Image Analysis Laboratory, [f]Micro-System and Micro-Fluidics Laboratory, [g]Clinical Systems and Signal Processing Organization, [h]Computational Biology and Biostatistics Laboratory, [i]Advanced Computing Laboratory, [j]Biomedical Imaging and Physiology Laboratory, [k]Applied Statistics Laboratory, [l]Molecular Imaging and Diagnostics Advanced Technologies, [m]Computer Vision Laboratory, [n]Software Science and Analytics Organization, and [o]Life Sciences and Molecular Diagnostics Laboratory, GE Global Research Center, Niskayuna, NY 12309; and [d]GE Healthcare, John F. Welch Technology Centre, 560066 Bangalore, India

Edited by Dennis A. Carson, University of California, San Diego, La Jolla, CA, and approved May 15, 2013 (received for review January 4, 2013)

Limitations on the number of unique protein and DNA molecules that can be characterized microscopically in a single tissue specimen impede advances in understanding the biological basis of health and disease. Here we present a multiplexed fluorescence microscopy method (MxIF) for quantitative, single-cell, and subcellular characterization of multiple analytes in formalin-fixed paraffin-embedded tissue. Chemical inactivation of fluorescent dyes after each image acquisition round allows reuse of common dyes in iterative staining and imaging cycles. The mild inactivation chemistry is compatible with total and phosphoprotein detection, as well as DNA FISH. Accurate computational registration of sequential images is achieved by aligning nuclear counterstain-derived fiducial points. Individual cells, plasma membrane, cytoplasm, nucleus, tumor, and stromal regions are segmented to achieve cellular and subcellular quantification of multiplexed targets. In a comparison of pathologist scoring of diaminobenzidine staining of serial sections and automated MxIF scoring of a single section, human epidermal growth factor receptor 2, estrogen receptor, p53, and androgen receptor staining by diaminobenzidine and MxIF methods yielded similar results. Single-cell staining patterns of 61 protein antigens by MxIF in 747 colorectal cancer subjects reveals extensive tumor heterogeneity, and cluster analysis of divergent signaling through ERK1/2, S6 kinase 1, and 4E binding protein 1 provides insights into the spatial organization of mechanistic target of rapamycin and MAPK signal transduction. Our results suggest MxIF should be broadly applicable to problems in the fields of basic biological research, drug discovery and development, and clinical diagnostics.

cancer diagnostics | high-content cellular analysis | image analysis | mTOR | multiplexing

Advances in molecular characterization technologies have radically affected cancer research, understanding, diagnosis, and treatment. For example, comprehensive genomic analysis shows that breast cancer can be divided into at least four intrinsic molecular subtypes, and each subtype is associated with a differential phenotype, prognosis, and response to therapy (1, 2). Comprehensive molecular profiling has also revealed intrinsic molecular subtypes of other cancers, including glioblastoma, squamous lung, colorectal, and ovarian cancers (3–6). These classifications promise to drive development of new diagnostics and inform therapy decisions. Although multigene-based tests facilitate interrogation of broad genomic profiles of the whole specimen, important histological, cellular, and subcellular context is lost. Continued advances in basic and translational cancer research will likely require new comprehensive molecular profiling technologies.

Motivated by the need to maximize biomarker data from costly drug discovery efforts and clinical trials, shrinking sample sizes, and increasing appreciation of disease complexity, the use of multiplexed molecular analysis has steadily increased (7). Formalin-fixed paraffin-embedded (FFPE) tissue is the most common form of preserved archived clinical sample. FFPE tissues are extensively used for routine diagnosis, and archived, clinically annotated FFPE specimens have been used successfully to identify prognostic and predictive cancer biomarkers in retrospective analyses (8–10). Chromogenic immunohistochemistry (IHC) is commonly used to determine in situ biomarker expression in FFPE tissue [e.g., diaminobenzidine (DAB) staining] but suffers from a number of inherent limitations, including the requirement of a new sample for each analyte, nonlinear staining intensity, and laboratory-to-laboratory variability due to subjective semiquantitative analysis (11).

Fluorescence microscopy enables limited multiplexed, quantitative analyses in cell and tissue specimens. Up to five fluorescent dyes can be spectrally resolved using standard optical filters, and separation of up to seven fluorophores has been reported with multispectral imaging (12). Despite these attributes, intrinsic autofluorescence often precludes detection of all but the most abundant molecules in fluorescence microscopy of FFPE tissues (13).

The limitations described above motivated us to develop an analytical technology capable of quantitative, high-dimensional, in situ data acquisition from biological tissue specimens (Fig. 1). In this report we describe a fluorescence microscopy procedure that enables high-level multiplexing of protein and nucleic acid detection

Author contributions: M.J.G., C.J.S., A. Sood, R.J.F., M.C.M., A.S.-P., B.D.S., and F.G. designed research; M.J.G., C.J.S., A. Sood, M.O.B., A.B., A. Can, S.D., D.H., S.K., K.K., M. Larsen, M. Lazare, Q.L., C.L., C.C.M., E.M., Z.P., A.S.-P., M.L.S., A. Seppo, and J.Z. performed research; M.J.G., C.J.S., A. Sood, M.O.B., A. Can, A. Corwin, S.D., R.J.F., V.K., K.K., C.C.M., Z.P., J.R., A.S.-P., B.D.S., K.S., Y.S., and F.G. contributed new reagents/analytic tools; M.J.G., C.J.S., A. Sood, S.A., Q.L., Z.P., Y.S., and F.G. analyzed data; and M.J.G., C.J.S., A. Sood, and F.G. wrote the paper.

Conflict of interest statement: All authors affiliated with GE Global Research Center, Niskayuna, NY, 12309 are current employees of General Electric Company.

This article is a PNAS Direct Submission.

Freely available online through the PNAS open access option.

[1]M.J.G., C.J.S., and A. Sood contributed equally to this work.

[2]Present address: Clinical Software Engineering, GE Healthcare Waukesha, WI 53188.

[3]Present address: MultiOmyx R&D Laboratory. Clarient: A GE Healthcare Company, Aliso Viejo, CA 92656.

[4]Department of Biological Sciences, State University of New York at Albany, Albany, NY 12222.

[5]Clinical and Medical Affairs Omnyx, LLC, Pittsburgh, PA 15212.

[6]To whom correspondence should be addressed. E-mail: ginty@research.ge.com.

This article contains supporting information online at www.pnas.org/lookup/suppl/doi:10.1073/pnas.1300136110/-/DCSupplemental.

and quantitation in a single FFPE tissue section. Image-processing algorithms register image stacks, remove intrinsic autofluorescence, segment individual cells and tissue compartments, and quantify subcellular expression levels of multiplexed molecular targets. We report several aspects of this technology, including combined immunofluorescence, H&E, and DNA FISH, a comparison of automated staining analysis to standard IHC in breast cancer, and single-cell analysis of 61 protein antigens in 747 human colorectal cancer specimens.

Results

Development of a Fluorophore Inactivation Solution. Because fluorescence analytical approaches limit the number of target measurements possible in a single tissue specimen, we developed an assay capable of exceeding these limits in multiple sample types, including FFPE tissues. Alkaline oxidation chemistry was developed that eliminates cyanine-based dye fluorescence within 15 min (U.S. patent 7,741,045) (14). The kinetics of fluorescence inactivation was measured via changes in optical absorbance (Fig. S1). After 5 min in dye inactivation solution, 60% and 80% reductions in absorbance were observed for Cy3 and Cy5, respectively (Fig. S1 *A* and *B*). A 15-min reaction with inactivation solution was sufficient to reduce fluorescence signals to less than 2% of original intensities. In corresponding control experiments, dyes showed no loss of absorption in PBS, and absorbance measurements of inactivated dyes returned to PBS confirmed the reaction is irreversible (Fig. S2). Additional fluorescent dyes were also evaluated (Fig. S1*C*). Unlike Cy dyes, absorbance spectra of DAPI, fluorescein (FITC), and ATTO495 remained unchanged after 30-min reactions with inactivation solution. Given DAPI's utility as a nuclear counterstain, we explored this finding further. DAPI's absorbance spectrum remained unchanged in 140-min reactions with the inactivation solution (Fig. S1*D*). Therefore, DAPI-stained nuclei can be imaged in each staining round and used as spatial reference points for registration, enabling quantitative analysis of image stacks (Figs. S3 and S4).

Sample Preparation and Dye-Cycling Conditions. We devised a routine process for sample analysis. Tissue was dewaxed and rehydrated using standard conditions, followed by a two-step antigen retrieval process that allows for application of antibodies that work optimally with acidic, basic, or protease-based antigen retrieval (U.S. patent 8,067,241) (15).

To address the possibility that dye inactivation would result in loss of target epitopes and/or tissue integrity, we examined four markers with distinct subcellular localization patterns after repeated dye-inactivation reactions. Cyanine 3 (Cy3)-labeled anti–β-catenin and cyanine 5 (Cy5)-labeled anti-α smooth muscle actin (SMA) were analyzed in breast tissue over 100 reaction cycles, and Cy3-labeled anti-cellular tumor antigen p53 (p53) and Cy5-labeled anti–pan-keratin were analyzed in colon tissue over 90 reaction cycles. A sample was stained and imaged at each 10-cycle interval of repeated 15-min incubations in inactivation solution and compared with an untreated control. In both tissue specimens we observed no difference in staining intensity after all cycles for β-catenin and SMA and p53 and pan-keratin (Fig. S5*D*), confirming no loss of target antigens or tissue integrity.

In this report, staining of 72 antibody–antigen pairs is described. Of these, 59 have been tested in series of 0, 1, 5, and 10 dye-inactivation reactions as part of routine antibody–antigen characterization (Fig. S5 *A*–*C* and Dataset S1); 51 were unaffected and 8 demonstrated some degree of sensitivity to the dye-inactivation chemistry. Seven of the eight were moderately affected and exhibited a lower signal intensity after one and five rounds of exposure, with staining still evident after 10 reactions. One target [ribosomal protein S6 (RPS6)] exhibited extreme sensitivity, with large decreases in staining intensity at one and five rounds, and almost complete elimination of signal by 10 rounds of dye inactivation. No predictable trend based on cellular localization or phosphorylation status was evident in susceptible antigen–antibody pairs.

Single-Cell Analysis and Visualization of Biological Features. We stained lineage-specific proteins such as epithelial cytokeratins, endothelial CD31, and SMA to define cancer tissue's cellular makeup with cellular resolution (Fig. 2*A* and Fig. S6). Immunostains demarcating the plasma membrane, such as anti-Na^+K^+ ATPase, and DNA stains of the nucleus further enabled delineation of tissue and cellular architecture at single-cell and subcellular resolution (Figs. 1 and 2 *D* and *C*). Pseudocolored, overlaid images were generated to visualize tissue architecture (Fig. 2*E*), and computational image analysis algorithms were used to generate segmentation masks for cellular and subcellular analysis of epithelial cells (16) (Figs. 1 and 2*F*).

We tested dye-cycling for compatibility with H&E staining of tissues at the end of the multiplexing cycle [eosin fluorescence precludes its use before multiplexed fluorescence microscopy (MxIF)]. DAPI images were computationally registered with hematoxylin-stained cell nuclei, allowing fluorescent images to be overlaid with the H&E image (Fig. S7) (17). Pseudocolored structural protein and DNA stains were also used to generate H&E-like images to aid in visualization and interpretation of tissue morphology (Figs. 2*G* and 3 *A*, *1*). Chromogen-like pseudocoloring of single stains was used to facilitate staining interpretation in a manner consistent with traditional DAB staining (Fig. 2 *H*).

Combined Immunofluorescence and DNA FISH. Combined analysis of nucleic acids and proteins from the same biological sample is of increasing importance in disease diagnosis (18). To test the utility of our dye-cycling method in combined analysis, breast cancer tissue samples were immunostained for human epidermal growth factor receptor 2 (HER2) and pan-keratin proteins, followed by DNA FISH analysis of the *HER2* gene. Tissue was probed with dye-labeled Cy5–anti-Her2 and Cy3–anti-pan-keratin antibodies and counterstained with DAPI (Fig. 2*I*). After dye inactivation, tissues were protease-treated followed by hybridization of dye-conjugated FISH probes for the *HER2* gene and centromere 17 (CEP17) as a reference marker. As expected, the CEP17 FISH probe produced two copies per nucleus in a majority of cells, and *HER2* probes in *HER2*-amplified tumors showed numerous clustered spots, which were detected with no apparent loss in sensitivity owing to the dye-cycling chemistry (Fig. 2*J*). Merger of HER2 protein and DNA FISH images allowed unambiguous comparison of DNA FISH with immunostaining of identical regions in the same sample (Fig. 2 *K* and *E*).

Multiplexed Analysis of Single-Cell Mechanistic Target of Rapamycin Signaling Phenotypes in Colorectal Cancer. Using MxIF, we examined complex phenotypes of established and emerging pathological features of colorectal cancer (CRC). Sixty-one protein antigens representing multiple signal transduction pathways and cellular aspects of tumor microenvironment were stained in specimens from 747 stage I–III CRC subjects distributed on three tissue microarrays (TMAs) (Dataset S2). The experiment included 38 distinct imaging steps. Each step was conducted on a single day, including staining. Thirty-two rounds included stains and six dispersed rounds were used to acquire autofluorescence signals for image processing (Dataset S3). The region of interest for each core was recorded once before iterative staining and imaging. Subsequent imaging steps included 15 min of manual operations to set exposure times and initialize imaging, followed by automated image acquisition. Staining required about 2 h of laboratory time, including the following steps:decover-slipping (15–30 min), manual staining (1 h at room temperature), manual rinses (15 min), and manual cover-slipping (15 min). Targets included markers of hypoxia and general cell stress, common pathological markers of CRC, as well as cellular features of tumor microenvironment including immune cells,

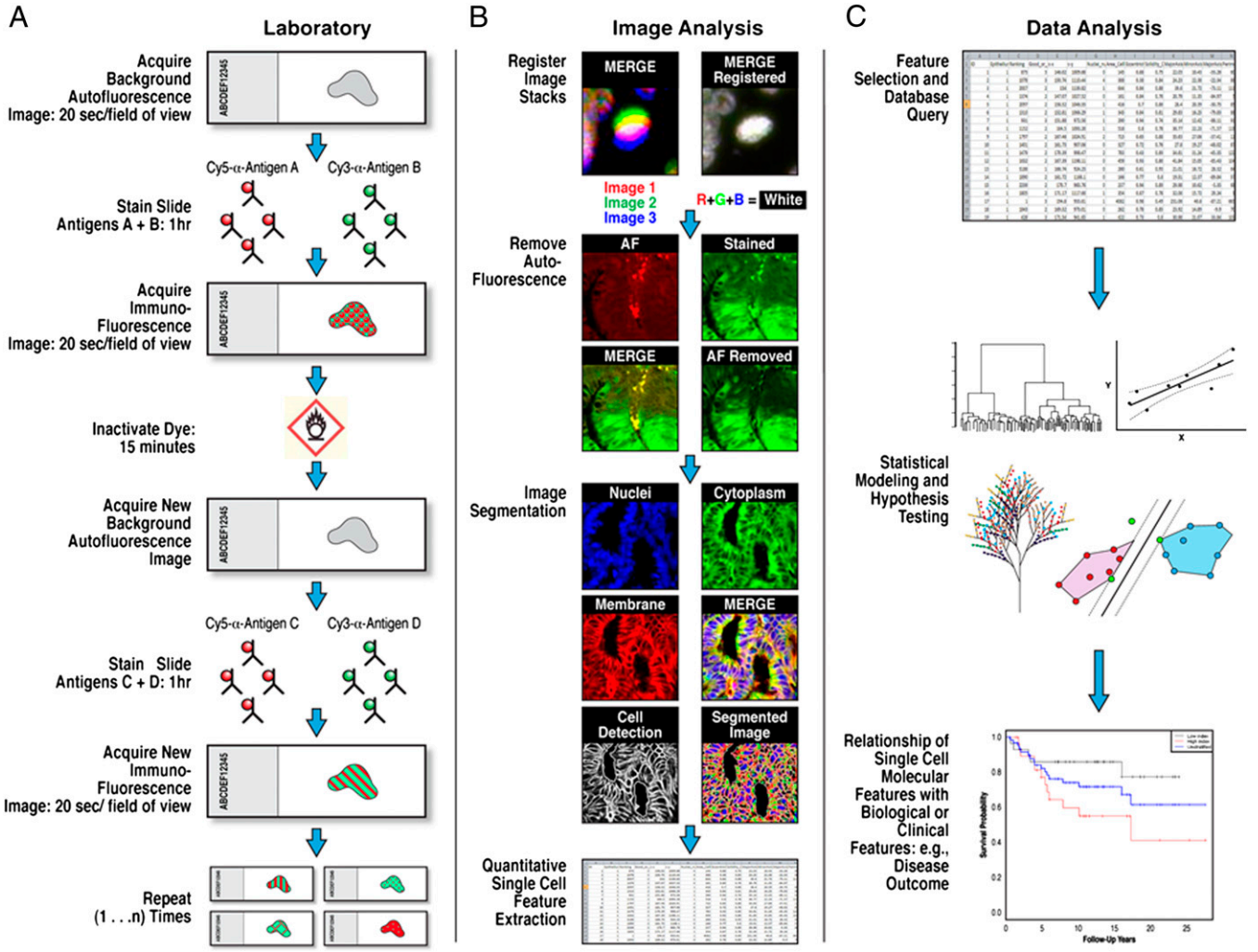

Fig. 1. MxIF data acquisition, image processing, and data analysis scheme. (*A*) In the laboratory, background autofluorescence (AF) tissue images are acquired before subsequent application of fluorescent dye-conjugated primary antibodies. Stained images are then acquired, followed by dye inactivation and restaining with new directly conjugated antibodies. New images are acquired, and the cycle is repeated until all target antigens are exhausted. Times associated with each step are indicated. (*B*) Stained images are registered, background AF is removed from each stained image, and images are segmented into epithelial and stromal regions, followed by identification of individual cells and corresponding plasma membrane, cytoplasm, and nuclear regions. Pixel-level data are summarized in cellular features, which is subsequently queried in data analysis (*C*). Data analysis can consist of a variety of statistical and visual explorations. In this work, we use K-median clustering to group cells with similar mTOR activity.

stromal cell markers, extracellular matrix, blood vasculature, and functional read-outs of several regulatory proteins and kinases (Dataset S3, Fig. 3, and Fig. S6). Positive staining of 44 antigens in a single specimen demonstrated important features of microenvironment, including endothelial cells, extracellular matrix, immune cells, fibroblasts, and additional signal transduction effectors (Fig. S6).

Kinases are important targets in the development of new anticancer therapies (19, 20). Mechanistic target of rapamycin (mTOR) is a kinase that regulates cellular growth. mTOR is dysregulated in a large proportion of human cancers and is under active clinical investigation as a therapeutic target (21, 22). Using MxIF to investigate one arm of the mTOR pathway in CRC cells, we analyzed phosphorylation levels of mTOR complex 1 (mTORC1) substrate eIF4E binding protein 1 (4E-BP1 T37/46) and ribosomal protein S6 (RPS6 S235/236), a substrate of the mTORC1 effector p70S6K (22, 23). MxIF staining of mTORC1-mediated RPS6 and 4E-BP1 phosphorylations revealed divergent signaling to 4E-BP1 and RPS6 in CRC tissues (Figs. 3 *B*, *1* and *2* and 4 *C* and *D*; Figs. S8 and S9). We expected to find positive correlations between mTORC1-associated RPS6 and 4E-BP1 phosphorylation on a subject level and single-cell basis, but visual analysis of composite images demonstrated frequent mutual exclusivity of these modifications (Figs. 3 *B*, *1* and *2* and 4; Figs. S8 *C* and *D* and S9 *A*–*C*).

Quantitative single-cell median intensity features were used to analyze RPS6, 4E-BP1, and ERK1/2 phosphorylation in individual cells from subjects with positive staining for at least one of these markers (Dataset S3). Of the 747 subjects studied, 20 did not stain positive for ERK1/2, RPS6, or 4E-BP1 phosphorylation. Antigens representing additional physiological processes were examined in negative cases to ensure sample integrity (Fig. S10). Robust staining of at least one modified site in a minimum of 50 cells was found in 436 subjects. These subjects were analyzed further. The average number of cells analyzed in each subject was 823 (median 405, SD 972, range 51–4,700). Using K-medians clustering of whole-cell-level RPS6, 4E-BP1, and ERK1/2 phosphorylations in epithelial tumor cells, we examined clustered cell groups for patterns of staining intensity of these three modifications in all 360,082 cells that stained positive for at least one of the above phosphorylations. Consistent with our

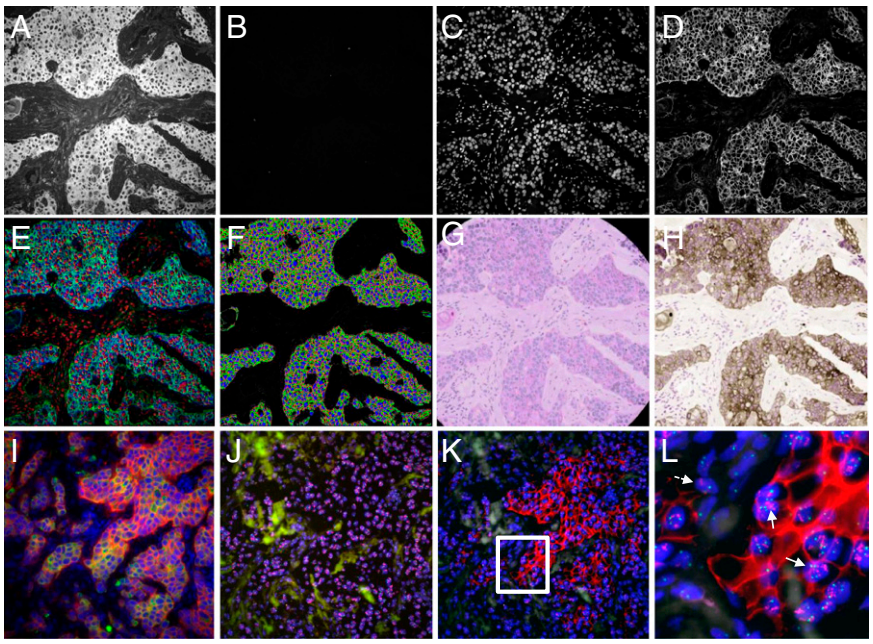

Fig. 2. Enhanced visualization of complex tissues and MxIF coupled with DNA FISH. Breast cancer tissue was stained and analyzed by the MxIF process: (*A*) Cytokeratin protein staining serves as epithelial cellular marker; (*B*) samples are imaged to confirm dye inactivation and generate background images used in the autofluorescence removal process; (*C*) DAPI signal is imaged every cycle and provides a reference for image registration; and (*D*) Na^+/K^+ATPase staining serves as a membrane marker for determining cell borders. Each fluorescent channel is pseudocolored, and after registration, a merged image can be generated (*E*). Segmentation maps are produced for subcellular specific analysis (*F*). An H&E-like representation of the tissue can be generated using selective color assignment of the fluorescent signals (*G*). Marker stains can be viewed with chromogen-like pseudocoloring (*H*) including hematoxylin-like nuclear counterstain from the DAPI signal. Combined staining with dye-conjugated antibodies and DNA FISH in breast cancer tissue shows pan-keratin and HER2 protein stains together with HER2 and CEP17 FISH. Pseudocolored composite images from a representative field of view at 40× magnification are shown as follows: (*I*) immunofluorescence for pan-keratin (green) and Her2 (red) with DAPI (blue); (*J*) FISH signals for HER2 (red), CEP17 (green), and DAPI (blue); (*K*) Her2 immunofluorescence (red) from first imaging round overlaid with HER2 FISH (purple), CEP17 FISH (green), and DAPI (blue); and (*L*) magnified view of the area marked in *K*, highlighting Her2 amplified cells (solid arrows) showing colocalization of HER2 gene amplification and Her2 protein expression, and normal cells (dashed arrow) with normal FISH pattern and undetectable Her2 protein signal.

visual interpretation, the first division in the hierarchical clustering dendrogram of 10 K-medians cell clusters divided cells with the highest levels of RPS6 phosphorylation from those with the highest level of ERK1/2 and 4E-BP1 phosphorylation (Fig. 4*A*). Cluster 3:10 was the only group with above average phosphorylation of all three targets, whereas cluster 5:10 displayed robust phosphorylation of both ERK and 4E-BP1 (Fig. 4*A*).

Analysis of cell cluster enrichment in each subject showed that the top enriched cluster in a notable proportion of subjects displayed mutual exclusivity in signaling through one arm of the pathway in the absence of the other [RPS6 top enriched: cluster 1 (6.7%) and cluster 4 (11.6%); 4E-BP1 top enriched: cluster 5 (1.7%), cluster 2 (5%), cluster 9 (16.7%), and cluster 7 (38%)] (Fig. 4*B* and Dataset S4). In contrast, only cluster 3 exhibited signaling at above average levels through both RPS6 and 4E-BP1 and was the top enriched cluster in just 2.3% of subjects analyzed (Fig. 4*B* and Dataset S4). These results confirm that high levels of RPS6 and 4E-BP1 phosphorylation largely occur independently at the cellular level.

RPS6 and 4E-BP1 phosphorylation were sometimes mutually exclusive in entire TMA cores representing thousands of cells from individual subjects. In subjects with cluster 2 enrichment (4E-BP1 phosphorylation high), 11/21 had zero cellular representation of robust RPS6 clusters 1, 3, and 4. Conversely, 13/50 cluster 4 enriched subjects (RPS6 phosphorylation high) are devoid of any cells from robust 4E-BP1 phosphorylation cell

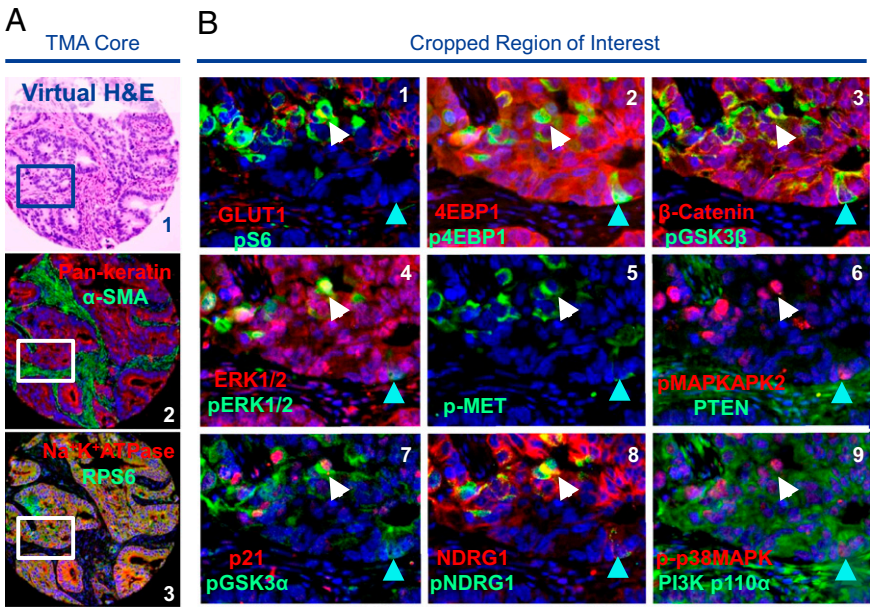

Fig. 3. Multiplexed immunofluorescence of signal transduction pathways in CRC. 747 FFPE stage I–III CRC specimens arrayed on three TMAs were stained for 61 protein antigens including markers of epithelial, immune and stromal cell lineage, subcellular compartments, oncogenes, tumor suppressors, and significant posttranslational protein modifications. Pseudocolored images of signaling and regulatory molecule staining in one small field of view are shown. Nuclei are counterstained with DAPI and pseudocolored blue in all images. (*A*, *1*) TMA core depicted in virtual H&E. (*A*, *2*) Pseudocolored overlaid immunofluorescence of epithelial cells stained positive for pancytokeratin and stroma area stained positive for α-smooth muscle actin. (*A*, *3*) Major subcellular compartments are detected by immunofluorescence staining of ribosomal protein S6 (cytoplasm) and Na^+K+ATPase (plasma membrane), and the nucleic acid stain DAPI (nucleus). (*B*) Activation of mitogenic and anabolic signaling pathways in CRC cells. Multiplexed immunofluorescence of signaling protein expression and phosphorylation shows complex activation and repression patterns of regulatory and signal transduction pathways. The white arrow indicates a single cell expressing each feature and the cyan arrow indicates a cell with differential expression of features.

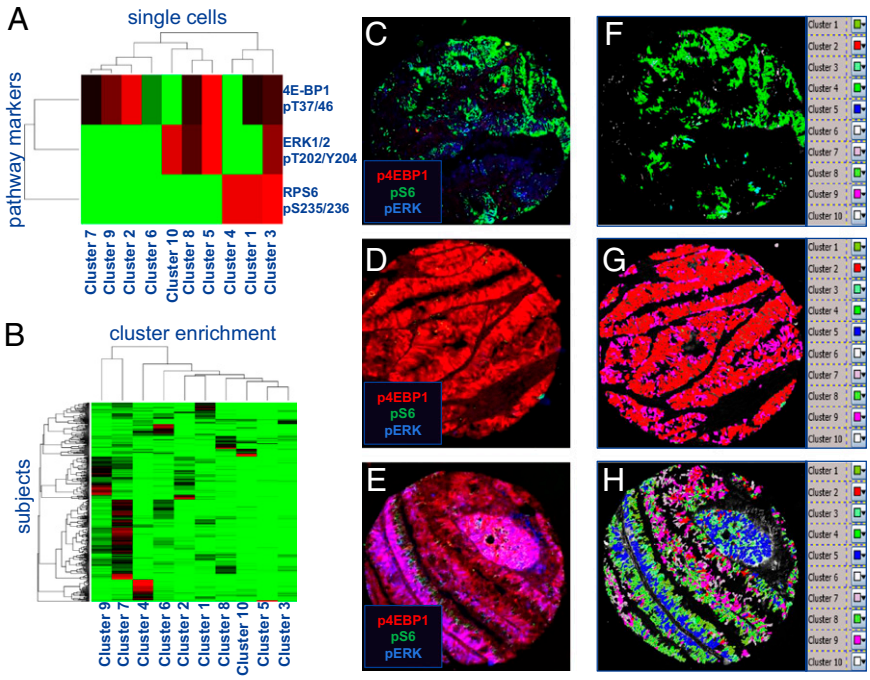

Fig. 4. Cluster analysis shows large-scale divergence of signaling to RPS6, 4E-BP1, and ERK1/2 in CRC cells. (*A*) K-medians clustering heat map of 4E-BP1 pThr37/46, RPS6 pSer 235/236, and ERK1/2 pT202/Y204 staining in 3.6×10^5 CRC cells from 720 subjects (abbreviated as p4EBP1, pS6, and pERK). (*B*) K-medians clustering heat map of enrichment in clusters from *A* in 436 subjects with ≥50 cells positive for p4E-BP1, pS6, or pERK. (*C*–*E*) Pseudocolor overlaid images of representative subjects enriched for mutually exclusive subject-level signaling (*C* and *D*) and a subject with many cell clusters (*E*) are shown. Mapping of cell clusters back on to images demonstrates cases exhibiting homogeneity (*F* and *G*) or heterogeneity (*H*) of cluster assignment. The legends in *F*–*H* show the colors selected to represent each cluster.

clusters, and 40/50 cluster 4 enriched subjects shared fewer than 5% of cells from any of the clusters with robust activation of 4E-BP1 (clusters 2, 3, 5, and 9) (Fig. 4 *A* and *B* and Dataset S4).

Because ribosomal S6 protein kinase (p90RSK) has been shown to phosphorylate RPS6 in an ERK1/2-dependent manner, we asked whether clusters with high levels of RPS6 phosphorylation were associated with high levels of activated ERK1/2 modifications at the single-cell level (24). In three of four cell clusters with above-average ERK1/2 phosphorylation, average RPS6 phosphorylation was negative, whereas cluster 3 was associated with high levels of RPS6 phosphorylation (Figs. 3 and 4 *A* and *B* and Fig. S9). However, cluster 3 was inconsistent with an exclusively mTORC1-independent, p90RSK-mediated RPS6 phosphorylation mechanism because it also exhibits above-average phosphorylation of 4E-BP1 (Fig. 4*A*). Further examination of the degree to which cell clusters with high levels of ERK1/2 activation coincide with the occurrence of clusters with high levels of RPS6 and 4E-BP1 phosphorylation at the subject level revealed little overlap between these clusters in the tumor regions analyzed (Fig. 4*B*). Taken together, these results suggest mTORC1 usually signals to these molecules under distinct spatiotemporal conditions in CRC cells, in vivo.

Discussion

In this work, we show that MxIF enables high-order, multiplexed, in situ microscopic analysis of biological molecules in individual cells. Although our applications focus on cancer, MxIF readily extends to tissue or cellular imaging research outside of oncology and should benefit many disciplines of basic and translational research and ultimately affect clinical practice.

Several limitations of current multiplexed fluorescence microscopy imaging technologies are overcome by MxIF. Attempting to catalog quantitative colocalized molecular features of cells with standard immunofluorescence methods becomes increasingly unfeasible as the number of analytes increases (e.g., to achieve all possible combinations of pairwise immunofluorescence of 61 proteins would require a prohibitive 1,830 samples). We detected 61 different protein epitopes in single FFPE tissue sections. An upper limit of analytes that can be examined in a single MxIF assay has not been reached. We also integrated MxIF with DNA FISH and H&E stains.

Our automated image analysis algorithms enable analysis of high-complexity cellular image data. Segmentation of tissue images into specific cell types and subcellular compartments facilitates quantitative subcellular biomarker localization measurements that agree with manual interpretation (Figs. S11 and S12). The repeated imaging of DAPI-stained nuclei provides fiducial points for each multiplexing round, allowing our registration algorithms to achieve accurate alignment of sequentially acquired images, which is vital to pixel-level analysis of molecular colocalization. We also developed algorithms to perform field flattening, autofluorescence removal, and regional, cellular, and subcellular quantitation of protein expression.

Alternative multiplexed microscopy strategies have been reported by others. Multiplexed imaging has been demonstrated by eluting or stripping antibodies with low pH or denaturation (25–27). Multiepitope ligand cartography (MELC) is a photobleaching technique to achieve dye cycling (28–30). The process has demonstrated imaging of 100 antigens in a single sample. Although MELC data allow analysis of protein networks within tissues, accompanying subcellular quantitation and integration with histological stains and DNA FISH have not been reported. Like the MELC approach, steric hindrance is generally not observed in our sequential antibody staining.

MxIF study of CRC allowed the mapping of cellular mTORC1 and MAPK signal transduction patterns in tissues with unprecedented resolution. Cluster analysis reveals that high-level phosphorylation of mTORC1-associated targets 4E-BP1 and RPS6 rarely occurs in the same cell, more often occurring in mutual exclusivity of one another. This likely reflects temporal or functional variation in mTORC1 signaling to these molecules, or cross-talk with other signaling pathways (Fig. S9 and Dataset S4). Taken together with the finding that MAPK signaling known to be upstream of RPS6 phosphorylation is rarely found in cells and subjects with robust phospho-RPS6^{high}/phospho-4E-BP1^{low} phenotypes, our data suggest contextually distinct mechanisms regulating mTORC1 signaling to these canonical downstream targets in human colorectal tumors (Fig. 4 and Figs. S6 and S9). In line with these findings, emerging experimental models of mTOR signaling suggest that cells differentially regulate canonical processes downstream of mTORC1. Recent work dissecting mTOR

function by genetic and pharmacological means shows that mTORC1 signaling through established targets S6K1 and 4E-BP1 can be regulated in distinct manners and influence different cellular functions (31). Rapamycin fails to inhibit mTORC1-mediated 4E-BP1 phosphorylation in many contexts, suggesting mTORC1 uses discrete mechanisms or binding partners to interact with its substrates (32). Our findings should be examined in model systems to better understand the functional significance of these divergences.

Our method combines data from morphological, protein, and DNA FISH-based analyses using a single sample. Automated segmentation and quantitation of fluorescence images enables standardization and assay robustness. The preservation of sample integrity and the combination of H&E imaging with molecular marker information maximizes molecular data from limited sample resources. Single-cell and subcellular analysis and cell clustering algorithms allowed identification of clusters that were relatively rare in the overall population (range 1.2–16.4%), demonstrating the utility of this approach in finding rare cell phenotypes such as transient signaling events. Furthermore, this platform allows characterization of additional features of interest such as cancer stem cells and tumor microenvironment, enabling high-content analysis of human tissues and extending established high-throughput in vitro cellular imaging methods.

Materials and Methods

Descriptions of additional results are included in *SI Results*, Specimens were acquired in adherence to institutional guidelines, Reagents, fluorescence microscopy hardware, immunofluorescence and FISH techniques, image processing, image and data analysis, antibody conjugation chemistry, and dye inactivation procedures are given in *SI Materials and Methods*.

ACKNOWLEDGMENTS. We graciously acknowledge the late Dr. William Gerald for providing valuable insight into tissue-based biomarker detection and the tissue arrays and stained slides for the pathologist's comparison study. We also thank Brian Ring (Clarient Inc.) and Rodney Beck, Douglass T. Ross, and Robert Seitz (formerly of Clarient Inc.), for providing colorectal cancer TMAs. Additionally, we acknowledge funding support, valuable discussions, and scientific input during the development of this work from Anirban Bhaduri, Christoph Hergersberg, John Burczak, Tom Treynor, Maureen Breshnahan, Jenifer Haeckl, and Dileep Vangasseri; and thank Tricia Tanner for significant editorial support during the manuscript writing process.

1. Anonymous; Cancer Genome Atlas Network (2012) Comprehensive molecular portraits of human breast tumours. *Nature* 490(7418):61–70.
2. Sørlie T, et al. (2001) Gene expression patterns of breast carcinomas distinguish tumor subclasses with clinical implications. *Proc Natl Acad Sci USA* 98(19):10869–10874.
3. Anonymous; Cancer Genome Atlas Research Network (2011) Integrated genomic analyses of ovarian carcinoma. *Nature* 474(7353):609–615.
4. Kwan ML, et al. (2009) Epidemiology of breast cancer subtypes in two prospective cohort studies of breast cancer survivors. *Breast Cancer Res* 11(3):R31.
5. Verhaak RG, et al.; Cancer Genome Atlas Research Network (2010) Integrated genomic analysis identifies clinically relevant subtypes of glioblastoma characterized by abnormalities in PDGFRA, IDH1, EGFR, and NF1. *Cancer Cell* 17(1):98–110.
6. Hammerman PS, et al.; Cancer Genome Atlas Research Network (2012) Comprehensive genomic characterization of squamous cell lung cancers. *Nature* 489(7417): 519–525.
7. Butcher EC, Berg EL, Kunkel EJ (2004) Systems biology in drug discovery. *Nat Biotechnol* 22(10):1253–1259.
8. Ring BZ, et al. (2006) Novel prognostic immunohistochemical biomarker panel for estrogen receptor-positive breast cancer. *J Clin Oncol* 24(19):3039–3047.
9. Ring BZ, et al. (2009) A novel five-antibody immunohistochemical test for subclassification of lung carcinoma. *Mod Pathol* 22(8):1032–1043.
10. Ross DT, et al. (2008) Chemosensitivity and stratification by a five monoclonal antibody immunohistochemistry test in the NSABP B14 and B20 trials. *Clin Cancer Res* 14(20):6602–6609.
11. Rimm DL (2006) What brown cannot do for you. *Nat Biotechnol* 24(8):914–916.
12. Tsurui H, et al. (2000) Seven-color fluorescence imaging of tissue samples based on Fourier spectroscopy and singular value decomposition. *J Histochem Cytochem* 48(5): 653–662.
13. Monici M (2005) Cell and tissue autofluorescence research and diagnostic applications. *Biotechnol Annu Rev* 11:227–256.
14. Gerdes MJ, et al. (2010) Sequential analysis of biological samples. US Patent: 7 741 045, issued June 22, 2010.
15. Gerdes MJ, Sood A, Sevinsky CJ (2011) Method and apparatus for antigen retrieval process. US Patent: 8 067 241, issued November 29, 2011.
16. Ginty F, et al. (2008) The relative distribution of membranous and cytoplasmic met is a prognostic indicator in stage I and II colon cancer. *Clin Cancer Res* 14(12):3814–3822.
17. Bello M, Tao X, Can A (2008) Accurate registration and failure detection in tissue micro array images. *Proceedings of the 2008 IEEE International Symposium on Biomedical Imaging: From Nano to Macro* (Inst Electrical Electronics Engineers, New York), pp 368–371.
18. Nitta H, et al. (2012) A gene-protein assay for human epidermal growth factor receptor 2 (HER2): Brightfield tricolor visualization of HER2 protein, the HER2 gene, and chromosome 17 centromere (CEN17) in formalin-fixed, paraffin-embedded breast cancer tissue sections. *Diagn Pathol* 7(1):60.
19. Jänne PA, Gray N, Settleman J (2009) Factors underlying sensitivity of cancers to small-molecule kinase inhibitors. *Nat Rev Drug Discov* 8(9):709–723.
20. Dar AC, Shokat KM (2011) The evolution of protein kinase inhibitors from antagonists to agonists of cellular signaling. *Annu Rev Biochem* 80:769–795.
21. Ma XM, Blenis J (2009) Molecular mechanisms of mTOR-mediated translational control. *Nat Rev Mol Cell Biol* 10(5):307–318.
22. Graff JR, et al. (2007) Therapeutic suppression of translation initiation factor eIF4E expression reduces tumor growth without toxicity. *J Clin Invest* 117(9):2638–2648.
23. Graff JR, et al. (2009) eIF4E activation is commonly elevated in advanced human prostate cancers and significantly related to reduced patient survival. *Cancer Res* 69(9):3866–3873.
24. Roux PP, et al. (2007) RAS/ERK signaling promotes site-specific ribosomal protein S6 phosphorylation via RSK and stimulates cap-dependent translation. *J Biol Chem* 282(19):14056–14064.
25. Glass G, Papin JA, Mandell JW (2009) SIMPLE: A sequential immunoperoxidase labeling and erasing method. *J Histochem Cytochem* 57(10):899–905.
26. Pirici D, et al. (2009) Antibody elution method for multiple immunohistochemistry on primary antibodies raised in the same species and of the same subtype. *J Histochem Cytochem* 57(6):567–575.
27. Wählby C, Erlandsson F, Bengtsson E, Zetterberg A (2002) Sequential immunofluorescence staining and image analysis for detection of large numbers of antigens in individual cell nuclei. *Cytometry* 47(1):32–41.
28. Friedenberger M, Bode M, Krusche A, Schubert W (2007) Fluorescence detection of protein clusters in individual cells and tissue sections by using toponome imaging system: sample preparation and measuring procedures. *Nat Protoc* 2(9):2285–2294.
29. Schubert W, et al. (2006) Analyzing proteome topology and function by automated multidimensional fluorescence microscopy. *Nat Biotechnol* 24(10):1270–1278.
30. Schubert W, Gieseler A, Krusche A, Hillert R (2009) Toponome mapping in prostate cancer: Detection of 2000 cell surface protein clusters in a single tissue section and cell type specific annotation by using a three symbol code. *J Proteome Res* 8(6): 2696–2707.
31. Hsieh AC, et al. (2010) Genetic dissection of the oncogenic mTOR pathway reveals druggable addiction to translational control via 4EBP-eIF4E. *Cancer Cell* 17(3): 249–261.
32. Choo AY, Yoon SO, Kim SG, Roux PP, Blenis J (2008) Rapamycin differentially inhibits S6Ks and 4E-BP1 to mediate cell-type-specific repression of mRNA translation. *Proc Natl Acad Sci USA* 105(45):17414–17419.

Supporting Information

Gerdes et al. 10.1073/pnas.1300136110

SI Results

Comparison of Multiplexed Fluorescence Microscopy Analysis and Pathologist Scoring of Breast Cancer Markers. We investigated whether our automated scoring process was consistent with pathologists' immunohistochemistry (IHC) scoring (1). Four markers commonly used in breast cancer diagnosis [estrogen receptor (ER), androgen receptor (AR), cellular tumor antigen p53, and human epidermal growth factor receptor 2 (Her2)] along with segmentation markers pan-cadherin, DAPI, and pan-keratin were multiplexed on a breast cancer tissue microarray (TMA). Four additional sequential TMA sections were diaminobenzidine (DAB)-stained for ER, AR, p53, and Her2 individually. Digital images of DAB-stained slides were captured and scored independently by two pathologists using conventional metrics (ER, AR, and p53 were positive when >10% nuclear staining was observed). Her2 was assessed as 0 (no staining), +1 (weak membrane staining), +2 (moderate membrane staining), or +3 (strong membrane staining). For data analysis, Her2 scores were binarized into 0 (0 and +1 patients) and 1 (+2 and +3 patients). Multiplexed fluorescence images were registered and background autofluorescence was subtracted, followed by computational segmentation of cancer cells to identify membrane, cytoplasm, and nuclei using pan-cadherin, pan-keratin, and DAPI, respectively (1). To examine whether order of antibody application affects staining results, we evaluated 11 stains on a breast cancer TMA and found no influence of staining order (Fig. S11).

Two different approaches were used to quantify MxIF staining: (*i*) The Kolmogorov–Smirnov test was used to determine subcellular localization patterns in comparison with reference distributions of segmentation marker staining and (*ii*) mean compartmental intensity to determine absolute signal measurements (nuclear for AR, ER, p53, and membranous for Her2). Receiver operating characteristic (ROC) analysis was used to compare the automated scores to the pathologists' assessments of the DAB-stained TMA, in which the area under the ROC curve was used as a measure of overall concordance. The threshold that maximizes sensitivity and specificity corresponding to the point on the ROC curve closest to (0.0, 1.0) was selected as the cutoff score. The median cutoff score was derived from the above ROC analysis of 100 bootstrap replicates for robustness. Automated scores were compared with scores generated by pathologists (Fig. S12 *A–D*). ER, p53, and Her2 demonstrate a high degree of concordance between the two methods [ER area under the curve (AUC) = 0.99; p53 AUC = 0.89; Her2 AUC = 0.83]. AR exhibits slightly lower concordance (area under the ROC = 0.76). Visual inspection of the DAB and multiplexed fluorescence microscopy (MxIF) images shows that some of the discrepancies could be attributed to lack of tissue, no staining in corresponding DAB or fluorescence images, or differences in staining localization (e.g., cytoplasmic staining of AR observed in some fluorescent images is not scored by pathologists). Overall, our automated multiplexed analysis yields results similar to manual pathologist scoring.

SI Materials and Methods

Tissue Specimens and Assessments. Adult human tissue samples were obtained as tissue slides embedded in paraffin. All tissues were procured and analyzed under institutional review board approval from the relevant institution. The tissue samples included slides of normal colon, breast, and prostate as well as prostate cancer, colon adenocarcinoma, prostate adenocarcinoma, and breast adenocarcinoma. Single tissue specimens were obtained either from Biochain, Biomax, Pantomics, or Thermo Scientific Lab Vision. Breast cancer TMAs were kindly provided by William Gerald, (Memorial Sloan Kettering Cancer Center, New York, NY). Breast cancer TMAs consisted of two or more cores from patient samples either with AR-positive/negative (50 patients, 110 cores), ER-positive/negative (46 patients, 91 cores), p53-positive/negative (48 patients, 90 cores) or Her2 0, +1, +2, or +3 (47 patients, 107 cores) tumors. Individual TMAs were stained using traditional chromogenic detection on a Ventana automated tissue stainer. Scoring and review of the tissue arrays was performed on the digitized images by two independent pathologists. ER, AR, and p53 were assessed as described above.

Colorectal cancer TMAs were provided by Clarient Inc. The colorectal cancer cohort was collected from the Clearview Cancer Institute of Huntsville Alabama from 1993 until 2002, with 747 patient tumor samples collected as paraffin-embedded specimens. The median follow-up time of patients in this cohort is 4.1 y, with a maximum of over 10 y. Stage 2 patients comprise 38% of this cohort; stage 1 and 2 combined are 65% of total patients. TMAs were constructed from three specimens from each subject arrayed in three unique blocks, amounting to nine total TMAs. Summary clinical statistics are found in Dataset S4. One TMA from each subject was prepared for MxIF as described in *SI Materials and Methods*, *Antibody Staining* and stained for 61 antigens over 37 imaging rounds including six background autofluorescence image acquisitions in rounds 1, 5, 10, 19, 29, and 33. Dye-labeled antibodies were applied in all other rounds as described in Dataset S1.

Reagents. Alexa 488, BODIPY (D6184), and hydroxycoumarin (H1193) were obtained from Invitrogen; ATTO 495, ATTO 635, and ATTO 655 were obtained from ATTO-TEC; DY-734-NHS was purchased from Dyomics; and fluorescein cadaverine was obtained from Biotium Inc. Fluorescently tagged secondary antibodies were obtained from Jackson ImmunoResearch Laboratories, Inc. cyanine 3 (Cy3) and cyanine 5 (Cy5)-NHS esters used for direct antibody conjugation were obtained from GE Healthcare. Several dye-conjugated primary antibodies were obtained directly from the manufacturer (Sigma): Cy3-mouse anti-smooth muscle α actin (αSMA) clone 1A4 (C6198), Cy3-mouse–anti-β-catenin clone 15B8 (C7738), Cy3-mouse–anti-Myc proto-oncogene protein (c-Myc) clone 9E10 (C6594), Cy3-rabbit–anti-γ-tubulin (C7604), and Cy3-mouse–anti-vimentin clone V9 (C9080). The primary antibodies that were conjugated included mouse anti-α SMA clone 1A4 (A2547; Sigma), rabbit anti–β-catenin (C2206; Sigma), rabbit anti–β-actin clone 13E5 (4970; Cell Signaling), mouse anti–pan-keratin clone PCK-26 (C1801; Sigma), mouse anti-estrogen receptor-α, clone 1D5 (M 7047; DAKO), goat anti-vimentin (V4630; Sigma), mouse anti-androgen receptor clone AR441 (M3562; DAKO), rabbit anti-fibronectin clone F1 (1573-1; Epitomics), mouse anti–pan-keratin 8/18 clones K8.8 and DC10 (MS-1603; Thermo Scientific), and mouse anti–E-cadherin (Thermo Scientific). Rabbit anti-Her2/neu (RB-103; Thermo Scientific) was used in all studies except the final colorectal cancer study of 61 markers, which used rabbit anti-HER2 D8F12 (4290; Cell Signaling) in colorectal cancer analysis. Others included mouse anti-p53 clones DO-7 and BP53-12 (MS-738; Thermo Scientific), rabbit anti-pan cadherin (RB-9036; Thermo Scientific), rabbit anti–phospho-40S ribosomal protein S6 (S6) (Ser-240/244) (2215; Cell Signaling), rabbit anti–phospho-S6 (Ser-235/236) clone D57.2.2E (4858; Cell Signaling), rabbit anti-S6 (2217; Cell Signaling), mouse anti-platelet endothelial cell adhesion molecule (CD31) clone 89C2 (3528; Cell Signaling), rabbit anti-sodium-potassium-ATPase clone EP1845Y

(2047-1; Epitomics), mouse–anti-macrosialin (CD68) clone KP1 (MS-397; Thermo Scientific), mouse–anti-signal transducer CD24 (CD24) clone ML5 (555426; BD Biosciences), mouse anti–apoptosis regulator Bcl-2 (Bcl-2)-alpha clone 100/D5 (MS-123; Thermo Scientific), rabbit–anti-cyclin D1 clone SP4 (RM-9104; Thermo Scientific), rabbit–anti-epidermal growth factor receptor (EGFR) clone D38B1 (4267; Cell Signaling), rabbit–anti-antigen KI-67 (KI-67) (RB-1510; Thermo Scientific), rabbit–anti–phospho-MAP kinase-activated protein kinase 2 (MAPKAPK2) (Thr334) clone 27B7 (3007; Cell Signaling), rabbit-anti-phosphatidylinositol 4,5-bisphosphate 3-kinase catalytic subunit alpha isoform (PI3Kp110α) clone C73F8 (4249; Cell Signaling), rabbit–anti-phospho-mitogen-activated protein kinase 1/2 (ERK1/2) (Thr202/Tyr204) clone 20G11 (4376; Cell Signaling) and rabbit–anti-phospho-p38 MAP kinase (p38 MAPK) (Thr180/Tyr182) clone D3F9 (4511; Cell Signaling), rabbit anti–solute carrier family 2, facilitated glucose transporter member 1 (GLUT-1) (07-1401; Millipore), mouse anti-human serum albumin clone HAS-11 (a6684; Sigma), mouse anti-collagen type IV, 7S domain clone IV-4H12 (MAB3326; Millipore), mouse anti-cytokeratin 19 clone BA17 (14-9898; eBioscience), rabbit anti–eukaryotic translation initiation factor 4E-binding protein 1 (4E-BP1) clone 53H11 (96440; Cell Signaling), rabbit anti–4E-BP1 phospho Thr37/46 (2855; Cell Signaling), mouse anti-protein Wnt-5a (Wnt-5a) clone 34D10 (ab86720; Abcam), rabbit anti-forkhead box protein O1 (FOXO1) clone C29H4 (2880; Cell Signaling), rabbit anti-forkhead box protein O3 (FOXO3a) clone EP1949Y (2071-1; Epitomics), rabbit anti-DNA mismatch repair protein Mlh1 - MutL protein homolog 1 (MLH1) clone EPR3894 (2786-1; Epitomics), E-cadherin clone 24E10 (3195; Cell Signaling), rabbit anti-glycogen synthase kinase-3 alpha (GSK-3α) phospho-Ser21 clone 36E9 (9316; Cell Signaling), rabbit anti-glycogen synthase kinase-3 beta (GSK-3β) phospho-Ser9 clone EPR2286Y (2435; Epitomics), rabbit anti-lamin A/C clone EPR4100 (2966-1; Epitomics), rabbit anti-histone-lysine N-methyltransferase (EZH2) clone D2C9 (5246; Cell Signaling), mouse anti-retinal dehydrogenase 1 (ALDH1) clone 11 (6111195; BD Transduction Laboratories), rabbit anti-cytokeratin 15 (HPA023910; Sigma), rabbit anti-cyclin-dependent kinase inhibitor 1 (p21) clone 12D1 (2947; Cell Signaling), mouse anti-Claudin1 clone 1C5-D9 (wh0009076m1; Sigma), mouse anti-CD44 antigen v6 clone VFF-7 (BMS116; eBioscience), rabbit anti-Indian hedgehog clone EP1192Y (1910-1; Epitomics), rabbit anti-B-lymphocyte antigen CD20 (CD20) clone EP459Y (1632-1; Epitomics), rabbit anti-EGFR phospho-Tyr1173 clone 53A5 (4407; Cell Signaling), rabbit anti-N-myc downstream-regulated gene 1 protein (NDRG1) EPR5592 (5326-1; Epitomics), mouse anti-CD68 clone KP1 (MS-397-PABX ; Thermo Fisher), mouse anti-transketolase-like protein 1 clone 1C10 (MCA5455Z ; AbD Serotec), mouse anti-T-cell surface glycoprotein CD8 (CD8) clone DK25 (M7103; Dako), mouse anti-B-cell antigen receptor complex-associated protein alpha chain (CD79) clone HM57 (M7050; Dako), rabbit anti-hepatocyte growth factor receptor (MET) phospho-Tyr1349 clone EP2367Y (2319-1; Epitomics), rabbit anti-MET (S1354; Epitomics), rabbit anti-RAC serine/threonine-protein kinase 1/2/3 (Akt) clone C67E7 (4691; Cell Signaling), rabbit anti- carbonic anhydrase 9 (CA9) (PA1-16592; Pierce/Thermo), rabbit anti-cleaved caspase3 Asp175 clone 5A1E (9664; Cell Signaling), rabbit anti-ERK1/2 clone 137F5 (4695; Cell Signaling), rabbit anti-EPCAM EPR677 (2) (3668-1; Epitomics), rabbit anti-DNA mismatch repair protein MutS protein homolog 2 (MSH2) clone D24B5 (2017; Cell Signaling), mouse monoclonal anti-scavenger receptor cysteine-rich type 1 protein M130 (CD163) (NCL-CD163; Leica), rabbit anti-cyclinB1 clone Y106 (1495-1; Epitomics), mouse anti-prostaglandin G/H synthase 2 (COX2) clone COX 229 (35-8200; Invitrogen), mouse anti-proliferating cell nuclear antigen (PCNA) clone PC10 (2586; Cell Signaling), and mouse anti-p53 clone DO-7 (M7001; Dako). Donkey serum and bovine serum albumin (BSA) were obtained from Jackson ImmunoResearch. Antifade mounting media was made containing 90% (vol/vol) glycerol in 1× PBS with diazobicyclooctane (DABCO) and *n*-propyl gallate as antifade agents. Paraformaldehyde (16% wt/vol) was obtained from Electron Microscopy Sciences. All other common reagents were obtained from Sigma.

Antibody Labeling. For indirect detection of bound primary antibodies, species-specific Cy3-or-Cy5–conjugated donkey secondary antibodies were obtained from Jackson ImmunoResearch and used at a dilution of 1:250. Primary antibodies were directly conjugated to either Cy3-or-Cy5 (GE Healthcare) or purchased as the Cy3 conjugate (see above). If not supplied in purified form, Protein A or G HP SpinTrap or HiTrap columns (GE Healthcare) were used following the manufacturer's protocols to purify the antibody before conjugation. After purification, the concentration was adjusted to 0.5–1.0 mg/mL and the pH was adjusted to 8.2–9.0 with 1.0 M sodium bicarbonate to a final bicarbonate concentration of 0.1 M. A small amount of NHS–ester dye was dissolved in anhydrous DMSO and the concentration was determined by measuring the absorbance of a 1:250 dilution of dye stock in 1× PBS at the appropriate wavelength on a ND-1000 spectrophotometer (NanoDrop Technologies). The appropriate amount of reconstituted NHS dye was added to each reaction to yield a ratio of two, four, or six dye molecules per antibody and the reaction was left in the dark at room temperature. After 90 min, the reactions were terminated and buffer exchanged and purified using Zeba desalting columns (Pierce) that had been equilibrated with 1× PBS buffer. The conjugation efficiency (dyes/antibody) was measured on a ND-1000 spectrophotometer using the appropriate absorbance measurements and the following equations (assuming a 1-cm path length in the spectrophotometer). Dye concentration correction factors were included to measure [Ab]:

- $[\mathrm{Ab}](\mu\mathrm{M}) = (A_{280} - (0.08^{*}A_{550})/0.210$ for Cy3
- $[\mathrm{Ab}](\mu\mathrm{M}) = (A_{280} - (0.05^{*}A_{650})/0.210$ for Cy5
- $[\mathrm{Cy3}](\mu\mathrm{M}) = A_{550}/0.15$
- $[\mathrm{Cy5}](\mu\mathrm{M}) = A_{650}/0.25$
- $\mathrm{D/P} = \mathrm{Dye}(\mu\mathrm{M})/\mathrm{Ab}(\mu\mathrm{M})$

Solutions were stabilized with BSA (0.2%, final concentration) and azide (0.09%, final concentration). Fluorescence intensities were collected for direct conjugates by preparing 50 nM antibody solutions and reading intensities on a BioRad FX Imager using the appropriate filter sets. Antibody dilutions for staining tissue were determined empirically for each antibody.

Measurement of Dye Spectrum After Signal Inactivation. Optical density (OD) was used to monitor loss of dye absorbance and, hence, fluorescence inactivation. Ten microliters of dye was mixed with an equal volume of 2× concentrated inactivation solution. Two microliters of the mixed solution was loaded onto a ND-1000 Spectrophotometer (NanoDrop Technologies) and the OD was read over a full spectrum (200–750 nm). For kinetics studies, measurements were taken at 0-, 5-, 15-, and 30-min intervals.

Antibody Staining. Formalin-fixed paraffin-embedded (FFPE) tissue samples or tissue arrays were baked at 65 °C for 1 h. Slides were deparaffinized with Histochoice clearing agent (Amresco), rehydrated by decreasing ethanol concentration washes, and then processed for antigen retrieval. A two-step antigen retrieval method was developed specifically for multiplexing with FFPE tissues, which allowed for the use of antibodies with different antigen retrieval conditions to be used together on the same samples (2). Samples were then incubated in PBS with 0.3% Triton X-100 for 10 min at ambient temperature before blocking against nonspecific binding with 10% (wt/vol) donkey serum and 3% (wt/vol) BSA in 1× PBS for 45 min at room temperature. Primary antibodies were diluted to optimized concentrations (typical range 0.1–10 μg/mL) and applied for 1 h at room

temperature or overnight at 4 °C in PBS/3% (vol/vol) BSA. Samples were then washed sequentially in PBS, PBS-TritonX-100, and then PBS again for 10 min, each with agitation. In the case of secondary antibody detection, samples were incubated with primary antibody species-specific secondary Donkey IgG conjugated to either Cy3 or Cy5. Slides were then washed as above and stained in DAPI (10 μg/mL) for 5 min, rinsed again in PBS, then mounted with antifade media for analysis. For the dye cycling process, following image acquisition, coverslips were floated away from the samples by soaking the slides in PBS at room temperature.

Dye Inactivation in Tissue. The general dye inactivation protocol used with tissues or cells was as follows. After image acquisition from a round of staining, slides were immersed in PBS to allow the coverslip to float off the slide. Samples were further washed in PBS and PBS/0.3% TritonX-100 and then dye inactivation was performed as previously described in US patent 7,741,045 (3). Briefly, slides were immersed in an alkaline solution containing H_2O_2 for 15 min with gentle agitation at room temperature (3). After 15 min, the slide was washed again with PBS. The sample was then either imaged to check the efficacy of the dye inactivation or restained with another round of antibodies followed by another round of image acquisition.

Antibody Validation. We created a standard process for antibody qualification (Fig. S5). Antibodies are selected on the basis of (*i*) staining specificity and sensitivity in indirect immunofluorescence, (*ii*) compatibility with the two-step antigen retrieval method described above, and (*iii*) resilience in 1, 5, and 10 rounds of dye inactivation chemistry (Fig. S5). Specificity tests included (where applicable to the antibody) immunogen peptide blocking before incubation with tissue, drug-treated fixed cell lines, fixed cell lines with gene amplification or deletion, phosphatase treatment of samples to verify phosphospecificity, and visual inspection of expected localization patterns (Fig. S5). Fluorescent dyes are conjugated to the primary antibody at several initial dye substitution ratios and specificity of each conjugate is verified and sensitivity is compared with levels found in previous experiments (Fig. S5*C*).

FISH. Breast cancer tissue was prepared for IHC and stained using anti–Her2-Cy5 and anti–pan-keratin-Cy3 primary antibodies. After image acquisition and dye inactivation of the protein stains, samples were treated with 0.1% pepsin in 2 mM HCl for 10 min, rinsed in PBS, and fixed in 4% (wt/vol) formaldehyde in PBS for 10 min. Her2/Cep17 FISH hybridization and post-hybridization washes were carried out using the PathVysion kit according to the manufacturer's instructions (Abbott Molecular). Sample and probe codenaturation and subsequent overnight hybridization at 37 °C was carried out in a Thermobrite slide hybridizer (Abbott Molecular).

Microscopy and Image Acquisition. Images of stained samples used in figures were collected on a Zeiss Axiovision Z1 motorized stage microscope equipped with high-efficiency fluorochrome specific filter sets for DAPI, Cy3, Cy5, Cy7, eGFP, and CFP (Semrock). The Piezo X-Y automated stage is used for repeatedly returning to the same location on slides for each round of imaging. For multiplexed staining where colocalization was desired, the slide was stained with DAPI and fields of interest were imaged and stage coordinates were saved using the Axiovision Mark & Find software. The coordinates of each image field were then recalled for each subsequent round after minor readjustment using reference points from the first-cycle DAPI image and determining the appropriate offset. Fluorescence excitation was provided by a 300-W xenon lamp source (Sutter Instrument). Images were captured with a Hamamatsu ORCA-IR CCD camera using Zeiss Axiovision software with initial exposure settings determined automatically within 75% saturation of pixel intensity. When comparing across samples, exposure times were set at a fixed value for all images of a given marker. For image analyses, microscopy images were exported as full resolution TIFF images in grayscale for each individual channel collected. Images were analyzed using either an average intensity measurement above threshold (OTSU algorithm), or as a ratio of signal: background intensities (minimum of 10 image fields per region of interest were selected).

Images from Figs. 1, 3, and 4 and Figs. S3–S6 and S8–S10 were obtained using an Olympus IX81 inverted fluorescence microscopy platform. The system was equipped with Prior illuminator–LumenPro 220 for florescence excitation, and an H117 ProScan Flat Top Inverted Microscope stage from Prior. DAPI, FITC (used for Cy2 imaging), Cy3, and Cy5 filters were from Semrock and matched to specifications for the equivalent filters used on the Zeiss platform. Images were acquired at 20× magnification using Olympus USPlanApo 20× 0.75 N.A. objective and QImaging Retiga 4000DC cooled CCD camera and saved as 12-bit grayscale TIFF images.

Image Preprocessing. The multiplexed experiments were set up such that nuclear (DAPI) images were acquired at each step. The nuclear images in each step were then registered to the nuclear images of a reference (typically the first) step, and images of all other channels were shifted accordingly. The rigid registration, involving only translation and rotation parameters, was performed in two steps. First, global translation parameters (no rotation) were computed using normalized correlation in the Fourrier domain. Normalized correlation guarantees a close-to-optimal solution even if the misalignment of the tissues is large from one step to another, and the computation was performed in the Fourier domain for speed benefits. In the second step, which involves rotation, a normalized mutual information metric was used for the registration, starting from the intial translation obtained by Fourier transform. Mutual information was robust to intensity differences between images. The description and validation of this procedure have been previously reported (4).

Autofluorescence, which is typical of FFPE tissues, needs to be properly characterized and separated from target fluorophore signals. We used autofluorescence removal processes that have previously been reported, wherein an image of the unstained sample is acquired in addition to the stained image (5, 6). The unstained and stained images are normalized with respect to their exposure times and the dark pixel value (pixel intensity value at zero exposure time). Each normalized autofluorescence image is then subtracted from the corresponding normalized stained image.

Regional Image Segmentation and Marker Quantification. For the purposes of subcellular quantitation, a segmentation algorithm was developed to identify membrane, cytoplasm, and nuclei using pan-cadherin and DAPI images (1). Using a method of quantification based on a probability distribution score generator (1), scores based on marker location were then determined (7, 8).

Single-Cell Segmentation and Quantification. Cell segmentation was performed by the following steps: (*i*) alignment of all of the image sets via DAPI-stained nuclei (7), (*ii*) removal of autofluorescence using an unstained image of each field of view, and (*iii*) reconstruction of the epithelial tissue architecture at the cellular and subcellular level. The epithelial tissue reconstruction algorithm performs hierarchical tissue segmentation in terms of individual epithelial cells and further performs subcellular cell segmentation on a cell-by-cell basis. The epithelial region was segmented using the staining pattern produced by either pan-cytokeratin or E-cadherin antibodies (breast and colon work, respectively). We detected the plasma membrane using a combination of the staining patterns represented by membrane proteins Na^+/K+-ATPase and pan-cadherin. Using a variation of a

watershed algorithm, we segmented individual cells, assigning a unique ID to each epithelial cell. Then, we applied a wavelet-based nucleus detection algorithm to segment the nuclei, and a variation of the probabilistic method described by Can et al. (9) to segment the membrane and cytoplasm. Therefore, we expressed the interior of each cell as nucleus, membrane, cytoplasm, and no detection. We digitally compartmentalized all epithelial cells in terms of (*i*) nucleus, (*ii*) membrane, and (*iii*) cytoplasm using the markers DAPI, Na^+K^+-ATPase, and ribosomal protein S6 (RPS6), respectively, and the detection algorithms previously described (7). A similar image analysis routine was previously applied to a study on Met distribution in colon cancer patients (1).

Once the basic subcellular segmentation was performed, we created two types of multiclass subcellular segmentation: (*i*) overlap and (*ii*) maximum compartment likelihood. In the overlap method, we assign multiple subcellular compartments to each pixel (if detected). In the maximum compartment likelihood, we assign each pixel to the subcellular compartment for which we find the maximum probability to belong to a given subcellular compartment along with a hierarchical voting scheme where segmented membrane has highest vote, followed by the nucleus and cytoplasm. Thus, we assign a unique subcellular compartment (nuclei, membrane, or cytoplasm) to each detected pixel.

We quantified both morphological (cell level) and protein-specific features (subcellular level) in the epithelial cells. We computed a number of morphological features describing the overall cell morphology, such as ellipticity, solidity, area, perimeter, number of nuclei (cells may not contain nuclei in FFPE tissue sections due to the plane of microtome cuts), area for (*i*) nuclei, (*ii*) membrane, and (*iii*) cytoplasm, and major and minor axis. Regarding protein quantification, we computed protein features from the autofluorescence-removed images with respect to (*i*) the entire cell, (*ii*) nuclei, (*iii*) membrane, and (*iv*) cytoplasm with respect to two quantification modes: (*i*) overlap and (*ii*) maximum compartment likelihood (described above). We computed different statistics, including mean, SD, maximum, and median protein expression of each protein with respect to the nucleus, membrane, and cytoplasm and entire cell. We therefore construct a 16-dimensional feature vector per cell and per protein quantifying the specific protein expression.

Statistical Analysis

Breast Pathologist/MxIF Concordance Assessment Study. Before final analysis of scores generated through the image analysis algorithms, stains were reviewed for general quality, integrity of tissue specimen, and finally the presence of epithelial structures and cells in the images. Sample cores where the tissue was either predominantly adipose or stroma were excluded.

Automated segmentation and scoring was used to measure the expression of the markers AR, ER, Her2, and p53 in the nucleus, cytoplasm and membrane compartments of the cell. For each marker, a DAB-stained TMA was used and a clinical pathologist determined the positivity of expression of the marker. Her2 scores were binarized to compose a negative group, Her2 0 and +1 patients, and a positive group, Her2 +2 and +3 patients. To assess the diagnostic validity of the automated scores, receiver operating curve (ROC) analysis (10, 11) was used to compare the automated scores to the pathologist's assessment of the DAB-stained TMA. Cutoff scores were determined similar to the method described in ref. 12 and used for MxIF stains in the breast cancer data to determine thresholds of positivity for AR, ER, Her2, and p53 expression on stained TMAs. A cutoff score was determined as the threshold on the automated score that maximizes both sensitivity and specificity [i.e., the threshold corresponding to the point on the ROC curve closest to (0.0, 1.0)]. Furthermore, to obtain a robust and reproducible cutoff score, the median cutoff from the above ROC analysis of 100 bootstrap replicates was used. Area under the ROC curve was used as a measure of overall concordance between manual and automated reads.

Colon Cancer Single-Cell Analysis. After segmentation, we used the median cellular protein expression levels of ERK1/2, RPS6, and eIF4E binding protein 1 (4E-BP1) site-specific phosphorylation in statistical analysis of the epithelial regions in all subjects. Cells were quality-controlled by applying the following filters:

i) Cell does not overlap the background (edge areas of the image with incomplete marker data due to misregistration).

ii) Cell has three or fewer segmented nuclei (mitotic cells and microtome artifacts lead us to select this parameter).

iii) Cell area contains 50–3,500 pixels [based on an exhaustive analysis of cells using the tracing and area measurement features in the image analysis software package ImageJ developed by Rasband and Ferreira (13)].

To better understand the pathway, only the cells that positively express at least one of the three proteins p4E-BP1, pS6235, and pERK are considered. The cutoff for positive staining was derived from a hand annotation of positively and negatively stained regions in a random selection of ~10% of all images in the study using imageJ (13). The subjects are arrayed on three slides. To make the proteins comparable across slides, quantile normalization was used. Every quantile of each protein expression on log2 scale for all of the cells on one slide is aligned to the corresponding quantile of the other slide.

After log2 transformation and slide quantile normalization, cells were clustered into K groups based on the three-dimensional marker space using K-medians clustering on 360,082 cells. The stepFlexclust function of flexclust library (v. 1.3-3) for R (v. 2.15.0) was run with 10 replicates assuming K ranged between 2 and 10. K-medians clustering algorithm uses Manhanttan distances between cells and then partitions cells into K groups and calculates the median for each cluster to determine its centroid. For each K, the initial centroids are randomly chosen and the minimum within-cluster distance solution is returned after 10 replicated runs.

Visualization of Cell Clusters on Cellular Images. Using in-house image visualization and analysis software, we made pseudocolored overlaid images of phosphorylated 4E-BP1, RPS6, and ERK1/2. We then used the software to assign different colors to 10 clusters derived from K-medians clustering described above and projected these clusters on the image to visualize their distribution and assess the veracity of the cluster assignments.

1. Ginty F, et al. (2008) The relative distribution of membranous and cytoplasmic met is a prognostic indicator in stage I and II colon cancer. *Clin Cancer Res* 14(12):3814–3822.
2. Gerdes MJ, Sood A, Sevinsky CJ (2011) Method and apparatus for antigen retrieval process. US Patent: 8 067 241, issued November 29, 2011.
3. Gerdes MJ, et al. (2010) Sequential analysis of biological samples. US Patent: 7 741 045, issued June 22, 2010.
4. Bello M, Tao X, Can A (2008) Accurate registration and failure detection in tissue micro array images. *Proceedings of the 2008 IEEE International Symposium on Biomedical Imaging: From Nano to Macro* (Inst Electrical Electronics Engineers, New York), pp 368–371.
5. Woolfe F, Gerdes M, Bello M, Tao X, Can A (2011) Autofluorescence removal by non-negative matrix factorization. *IEEE Trans Image Process* 20(4):1085–1093.
6. Pang Z, Laplante NE, Filkins RJ (2012) Dark pixel intensity determination and its applications in normalizing different exposure time and autofluorescence removal. *J Microsc* 246(1):1–10.
7. Can A, et al. (2008) Techniques for cellular and tissue-based image quantitation of protein biomarkers. *Microscopic Image Analysis for Lifescience Applications*, eds Rittscher J, Machiraju R, Wong STC (Artech House, London).
8. Can A, Bello M, Tao X, Seel M, Gerdes M (2008) TMA-Q: A tissue quality assurance tool for sequentially multiplexed TMAs. *Abstracts of the 3rd Intercontinental Congress of Pathology. Virchows Arch* 452(Suppl 1):S11 (abstr).
9. Can A, Bellow M, Cline HE, Tao X, Mendonca P, Gerdes M (2009) A unified segmentation method for detecting subcellular compartments in immunofluroescently la-

beled tissue images. *International Workshop on Microscopic Image Analysis with Applications in Biology*. September 3–4, 2009. NIH Campus, Bethesda MD.
10. Pepe MS, Longton G, Anderson GL, Schummer M (2003) Selecting differentially expressed genes from microarray experiments. *Biometrics* 59(1):133–142.
11. Eng J (2005) Receiver operating characteristic analysis: A primer. *Acad Radiol* 12(7): 909–916.
12. Zlobec I, Steele R, Terracciano L, Jass JR, Lugli A (2007) Selecting immunohistochemical cut-off scores for novel biomarkers of progression and survival in colorectal cancer. *J Clin Pathol* 60(10):1112–1116.
13. Schneider CA, Rasband WS, Eliceiri KW (2012) NIH Image to ImageJ: 25 years of image analysis. *Nat Methods* 9(7):671–675.

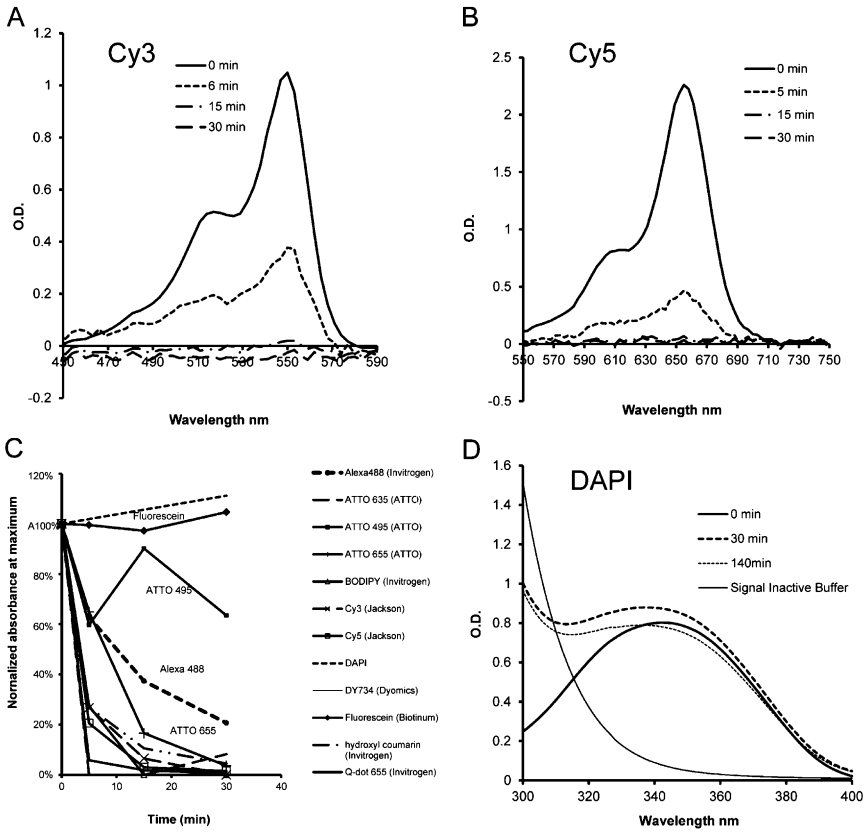

Fig. S1. Cyanine-based fluorescent dyes can be inactivated in solution, but DAPI is resistant. The kinetics of dye inactivation were evaluated by exposing Cy3 (*A*) and Cy5 (*B*) fluorophores to chemical dye-inactivation solution for 0, 5, 15, or 30 min. The full spectra ODs were then measured by spectrophotometer, and graphs of the ODs are shown. A panel of various other dyes (*C*) was also exposed to the inactivation solution for 0, 5, 15, or 30 min. A graph of the OD results is shown, in which the absorbance maximum for each sample was normalized. DAPI (*D*) was exposed to the inactivation solution for either 0, 30, or 140 min and the full spectra ODs were measured by spectrophotometer. A graph of the OD results is shown. Signal Inactive Buffer, dye-inactivation buffer alone.

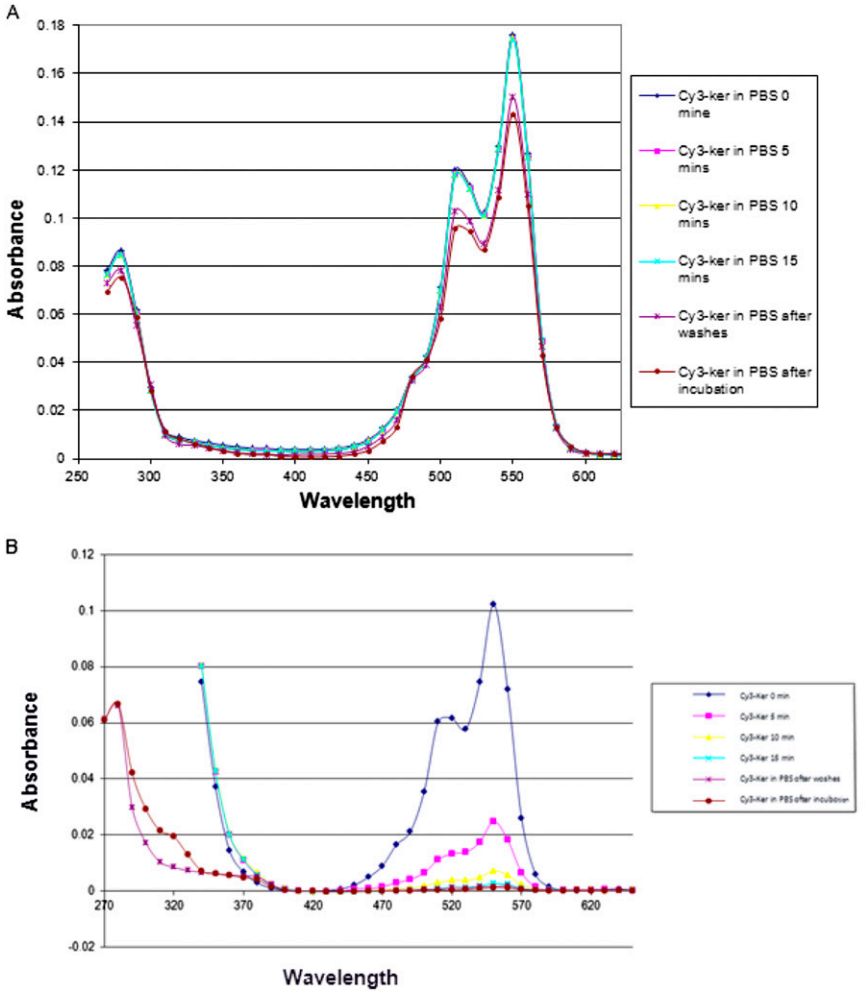

Fig. S2. Kinetics of dye inactivation. (*A*) Cy3-labeled keratin antibody was incubated in PBS to control for external loss of fluorescence. After all procedures there was no significant loss of fluorescence absorbance in controls. (*B*) Cy3-labeled keratin antibody was incubated in PBS or dye-inactivation solution and absorbance was monitored at 5-min intervals. After 15 min, the antibody was washed in PBS and measured, followed by an overnight incubation in the dark. After full inactivation at 15 min, there was no recovery of fluorescence.

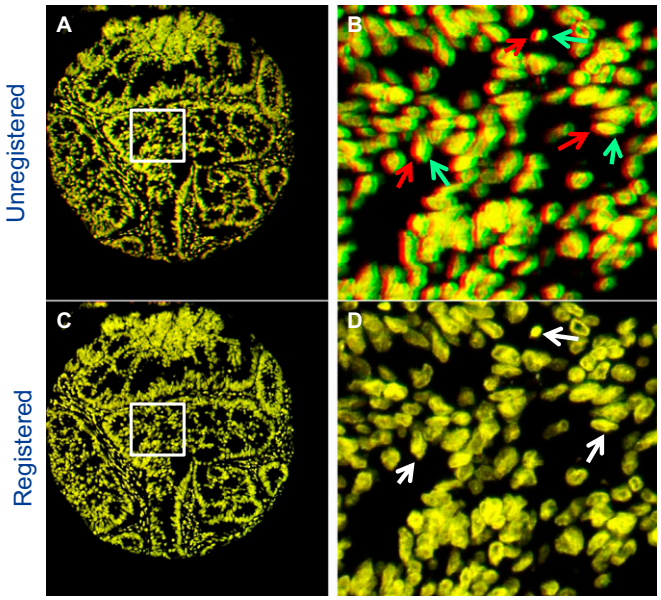

Fig. S3. Image registration. Iterative imaging of the same field of view requires realignment of consecutive images to enable pixel-level analysis of tissues. (*A* and *B*) DAPI-stained nuclei from two rounds of staining pseudocolored in red and green. (*B*) Red and green arrows illustrate gross misalignment. (*C* and *D*) Red and green pseudocolored DAPI-stained nuclei from different imaging rounds after image registration show colocalization, as indicated by a lack of red or green pixels and uniform yellow color indicative of consistent colocalized orientation of stained pixels (*D*).

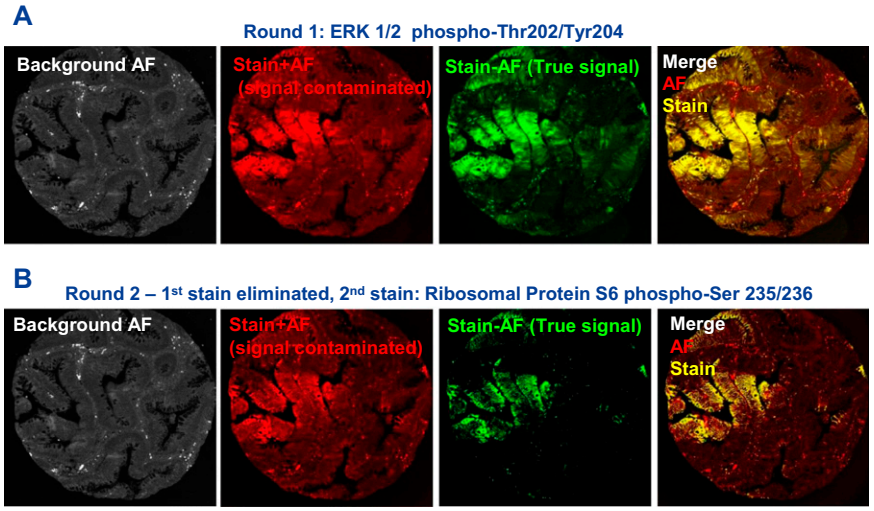

Fig. S4. Autofluorescence removal. (*A* and *B*) After image registration, a pixel-by-pixel subtraction of intrinsic autofluorescence removes contaminating signal, leaving signal derived from the molecular probe. The left-hand column shows images taken prior applying dye labeled probe, illustrating the baseline autofluorescence landscape. Dye-labeled probes are then applied to the tissue and imaged, shown in the second column. The autofluorescence (AF) image is then subtracted from the stained image to generate the AF-removed image in the third column. When the stained image is merged with the AF-removed image, as shown in the fourth column, areas of signal contamination are readily observed.

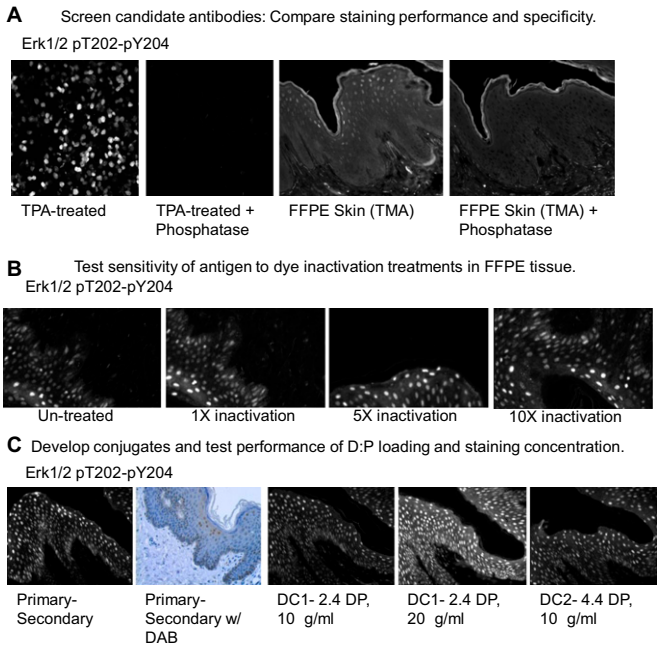

Fig. S5. (Continued)

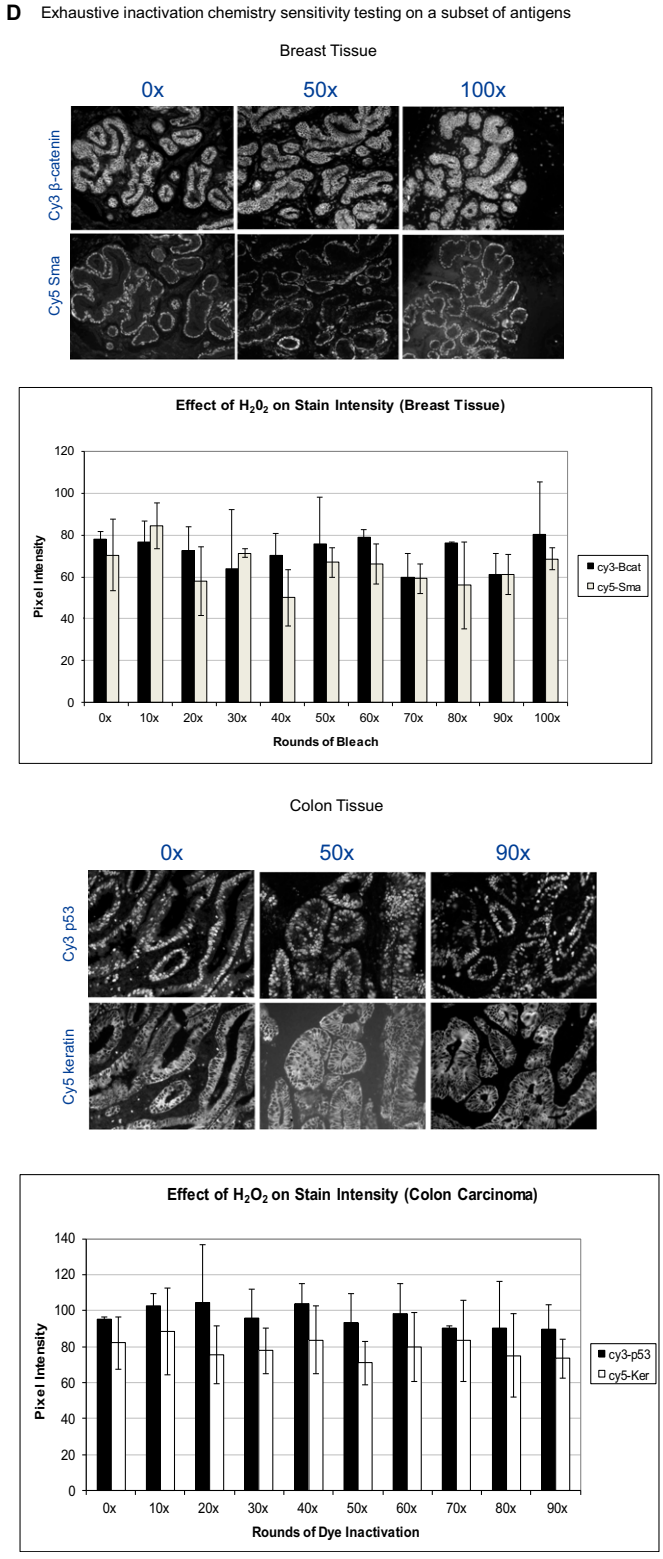

Fig. S5. Antibody validation and antigen dye-inactivation sensitivity testing. Specificity, antigenicity response to dye inactivation, and specificity of directly labeled antibodies are determined before certification of MxIF reagents. (*A*) Various specificity tests are used to verify antibody specificity. The left two images show phospho-ERK1/2 staining of FFPE 12-*O*-tetradecanoylphorbol 13-acetate (TPA)-treated NIH 3T3 cells with and without phosphatase treatment. Similar test are conducted in appropriate tissue specimens as shown in the right-hand images. (*B*) Tissues are then subjected to 1,5, and 10 rounds of dye-inactivation chemistry, and staining is compared with an untreated control. (*C*) Fluorescent dyes are covalently conjugated to the antibody, and resultant specificity and sensitivity are compared with unlabeled antibody staining. (*D*) Some antigens are tested against extended exposure to dye-inactivation chemistry. β-Catenin and smooth muscle actin epitopes in breast tissue are unaffected by 100 rounds of dye-inactivation chemistry; keratin and p53 epitopes in colon tissue are unaffected in 90 rounds of dye-inactivation chemistry.

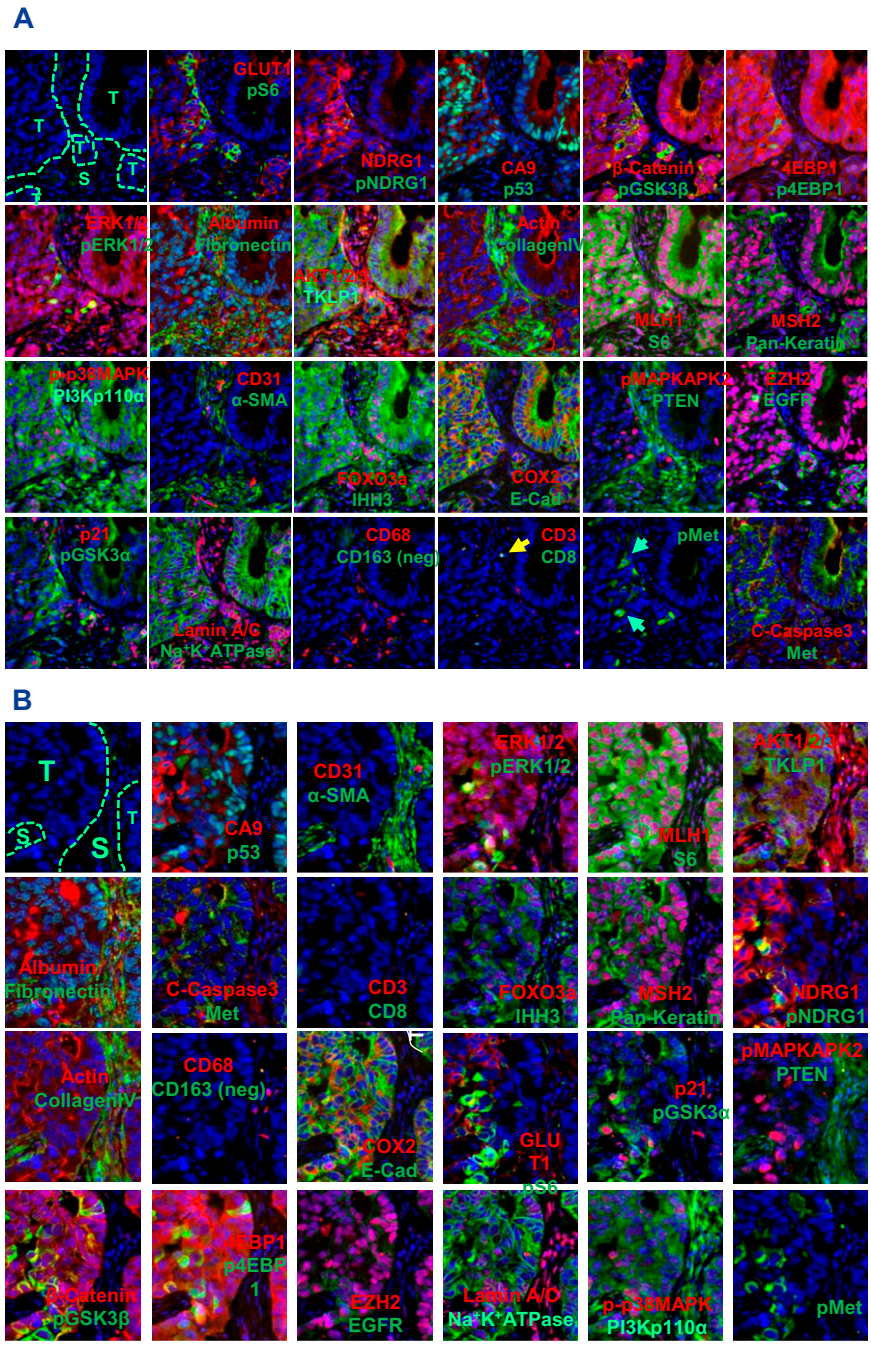

Fig. S6. Multiplexed immunofluorescence of tumor microenvironment in colorectal cancer. FFPE stage I–III colorectal cancer specimens ($n = 747$) assembled as 600- to 800-μm cores in three tissue microarrays were stained for 61 protein targets including markers of cell type, subcellular compartments, oncogenes, tumor suppressors, metabolic functions, and functionally significant posttranslational protein modifications. TMA cores were iteratively imaged at 20× magnification and pseudocolored overlaid images were generated. (*A* and *B*) Two fields of view with positive staining for 44/61 antigens stained are shown.

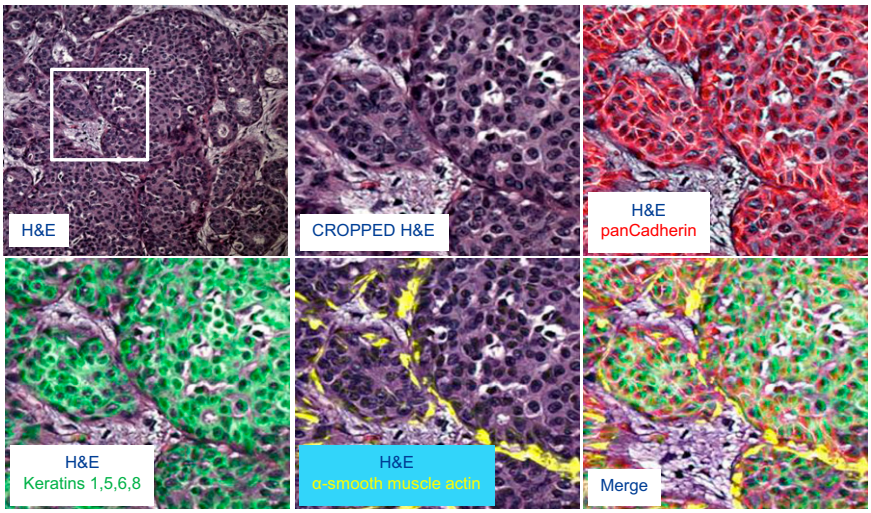

Fig. S7. Merger of H&E and MxIF. Standard H&E can be conducted after MxIF and registered to the molecular images for enhanced visualization and interpretation. A representative field of view was imaged for cadherin and keratin and dye was inactivated then imaged for α-smooth muscle actin staining. Dye was inactivated and H&E staining was conducted according to standard protocols. Hematoxylin- and DAPI-stained nuclei were registered and overlaid images created to allow combined histological and molecular viewing.

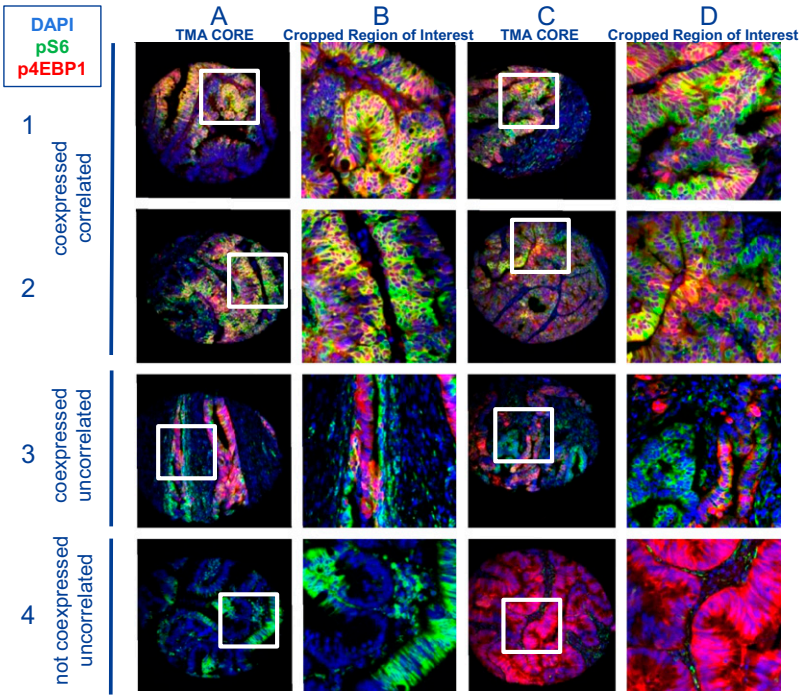

Fig. S8. Divergent signaling downstream of mechanistic target of rapamycin complex 1 (mTORC1) in colorectal cancer. Immunofluorescence of signaling downstream of mTORC1 reveals differential patterns of downstream signaling regulation in individual colorectal cancer cells, ranging from partially correlated to inversely correlated or not coexpressed. Pseudocolor images of registered and autofluorescence removed mTORC1 substrate 4EBP1 phosphothreonines 37/46 immunostaining and downstream p70S6K substrate RPS6 phosphoserines 235/236 immunostaining are overlaid with DAPI. Boxed regions in *A* and *C* are shown in higher magnification in *B* and *D*, respectively. (*1* and *2*) Colorectal tumors displaying robust mTORC1 signaling through 4EBP1 and RPS6. *A* and *C* are 600- to 800-μm cores from individual subjects and *B* and *D* are expanded regions of interest displaying mosaic staining for both modifications. (*3*, *A* and *B; 3*, *C* and *D*) Colorectal tumors displaying both modifications partitioned in a mutually exclusive cellular distribution. (*4*, *A* and *B*) A colorectal tumor displaying robust RPS6 phosphorylation in the absence of 4E-BP1 phosphorylation. (*4*, *C* and *D*) A colorectal tumor displaying high level 4E-BP1 phosphorylation in the absence of RPS6 phosphorylation.

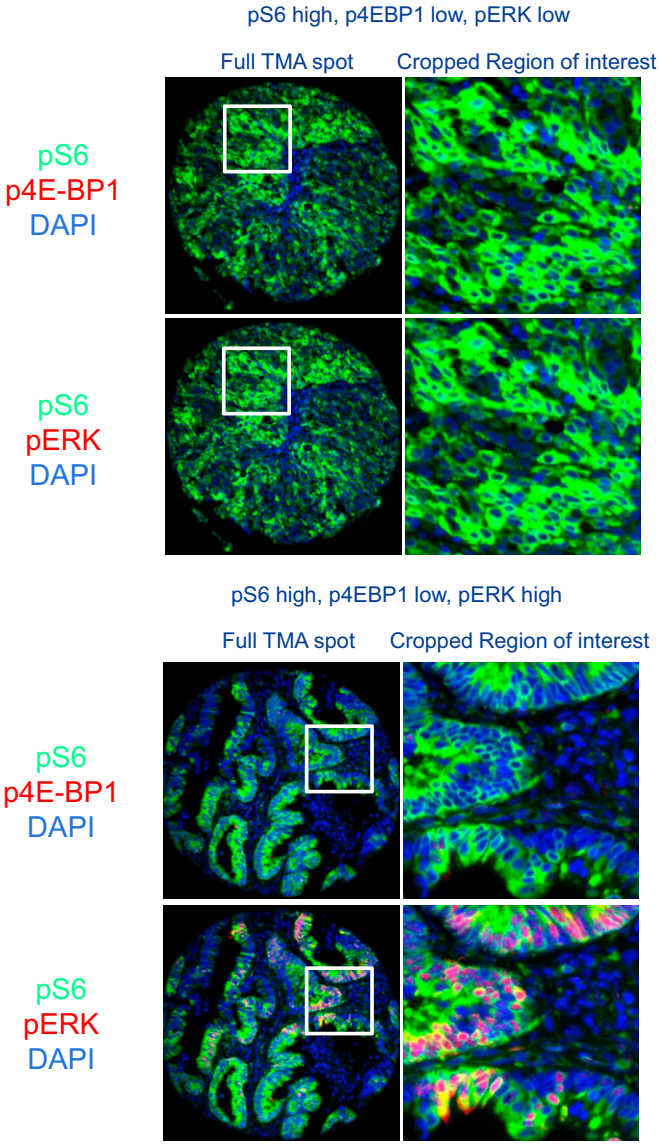

Fig. S9. MAPK/ribosomal S6 protein kinase (p90RSK) signaling is not active in many cases displaying exclusive signaling to S6 and not 4E-BP1. Analysis of MAPK signaling via p90RSK to S6 serines 235/236 cannot explain the majority of cases with robust S6 serine 235/236 phosphorylation and absent 4E-BP1 T37/S46 phosphorylation. (*Upper*) A case with robust pS6 with no staining for p4E-BP1 or pERK1/2, representing cell cluster 4, which shows mutually exclusive signaling to S6. (*Lower*) A tumor displaying robust MAPK activation in a case exhibiting exclusive signaling to S6 and not 4E-BP1.

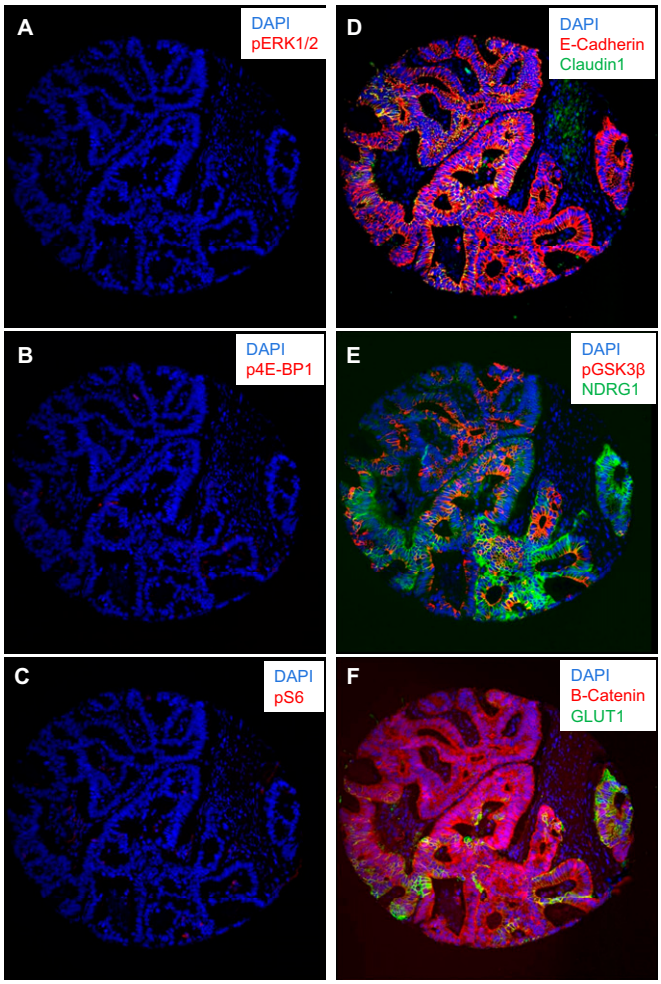

Fig. S10. Cases with no signaling to S6, 4E-BP1, or ERK1/2 phosphorlations targeted exhibit robust staining of other proteins and posttranslational modifications. On the left are overlays of DAPI with pERK, p4E-BP1, and pS6 from a single case exhibiting absence of signaling through these posttranslational modifications (*A*–*C*). In this same case, robust staining is observed for other proteins, including phospho-GSK3β serine 9, glucose transporter 1 (GLUT-1), N-myc downstream regulated 1 (NDRG1), E-cadherin, β-catenin, and Claudin-1 (*D*–*F*).

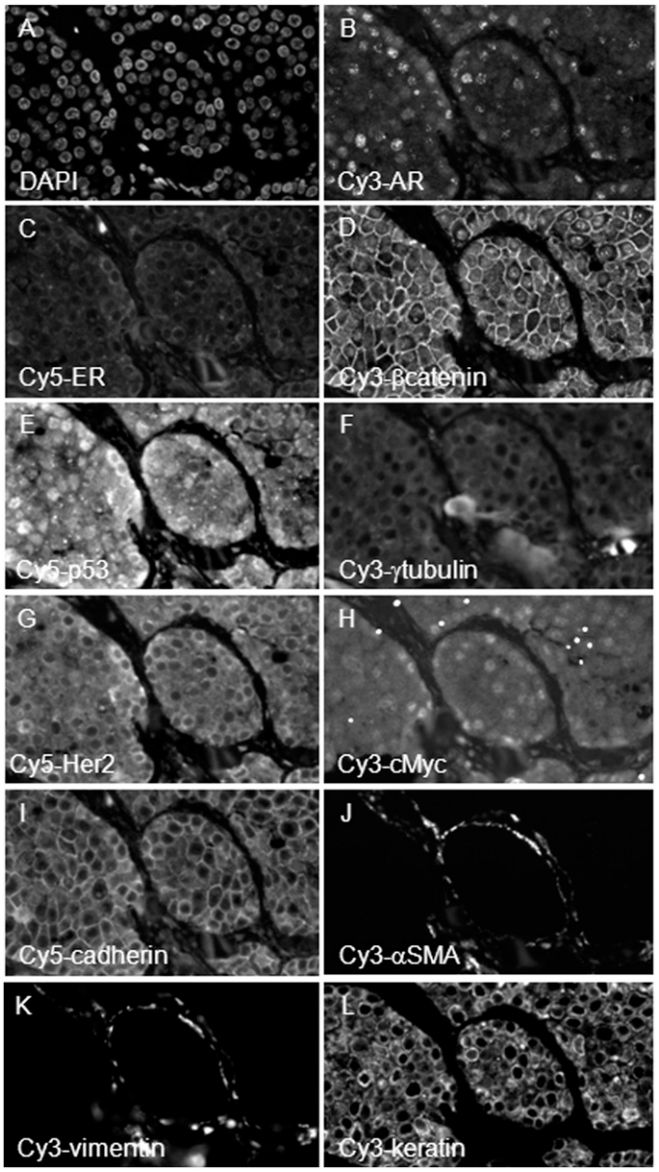

Fig. S11. Representative images from breast cancer pathologist comparison study. A set of 11 common breast cancer biomarkers were detected sequentially in breast cancer specimens in seven consecutive steps. Representative images for the markers include (*A*) DAPI, (*B*) AR, (*C*) ER (negative or equivocal), (*D*) β-catenin, (*E*) p53, (*F*) γ-tubulin, (*G*) Her2 (negative or equivocal), (*H*) c-MYC, (*I*) pan-cadherin, (*J*) α-SMA, (*K*) vimentin, and (*L*) pan-keratin.

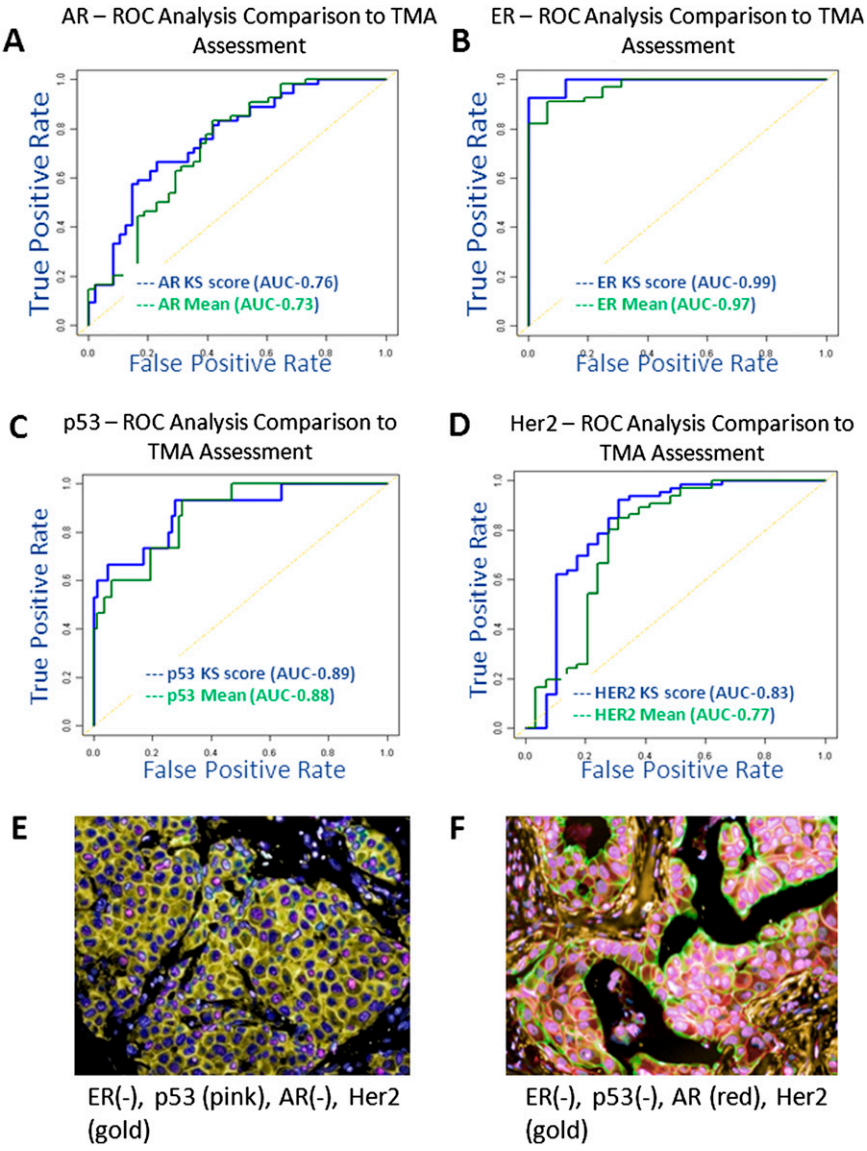

Fig. S12. Automated multiplexing analysis is consistent with manual pathologist scoring. Concordance of an automated multiplexing analysis with manual scoring was gauged by comparing the automated scores of various biomarker expression levels (AR, ER, p53, and Her2) with those obtained via manual pathologist assessment of a breast cancer TMA. ROC curves for each marker (*A–D*) were then generated as discussed in *SI Materials and Methods* to demonstrate the comparison between the two approaches. Visual assessment of merged pseudocolored images of Her2+/p53+ (*E*) and Her2+/p53− (*F*) tissue samples confirmed the expression patterns.

Dataset S1. Antibody information and dye Inactivation effects

Dataset S1

Dataset S2. Colorectal cancer cohort clinical characteristics

Dataset S2

Dataset S3. Colorectal cancer staining and imaging legend

Dataset S3

Dataset S4. Colorectal cancer cell data and cluster enrichment

Dataset S4